iScience

Article

Small molecule inhibitor binds to NOD-like receptor family pyrin domain containing 3 and prevents inflammasome activation

Activated Inflammasome | Inhibited Inflammasome

Angela Lackner,
Julia Elise Cabral,
Yanfei Qiu, ...,
Sophia Lin, Emy
Armanus, Reginald
McNulty

rmcnulty@uci.edu

Highlights

NLRP3 has a protein fold
similar to hOGG1 and can
cleave Ox-mtDNA

HOGG1 drugs TH5487 and
SU0268 bind to NLRP3 and
prevent interaction with
Ox-mtDNA

HOGG1 drugs TH5487 and
SU0268 prevent NLRP3
inflammasome activation in
macrophages

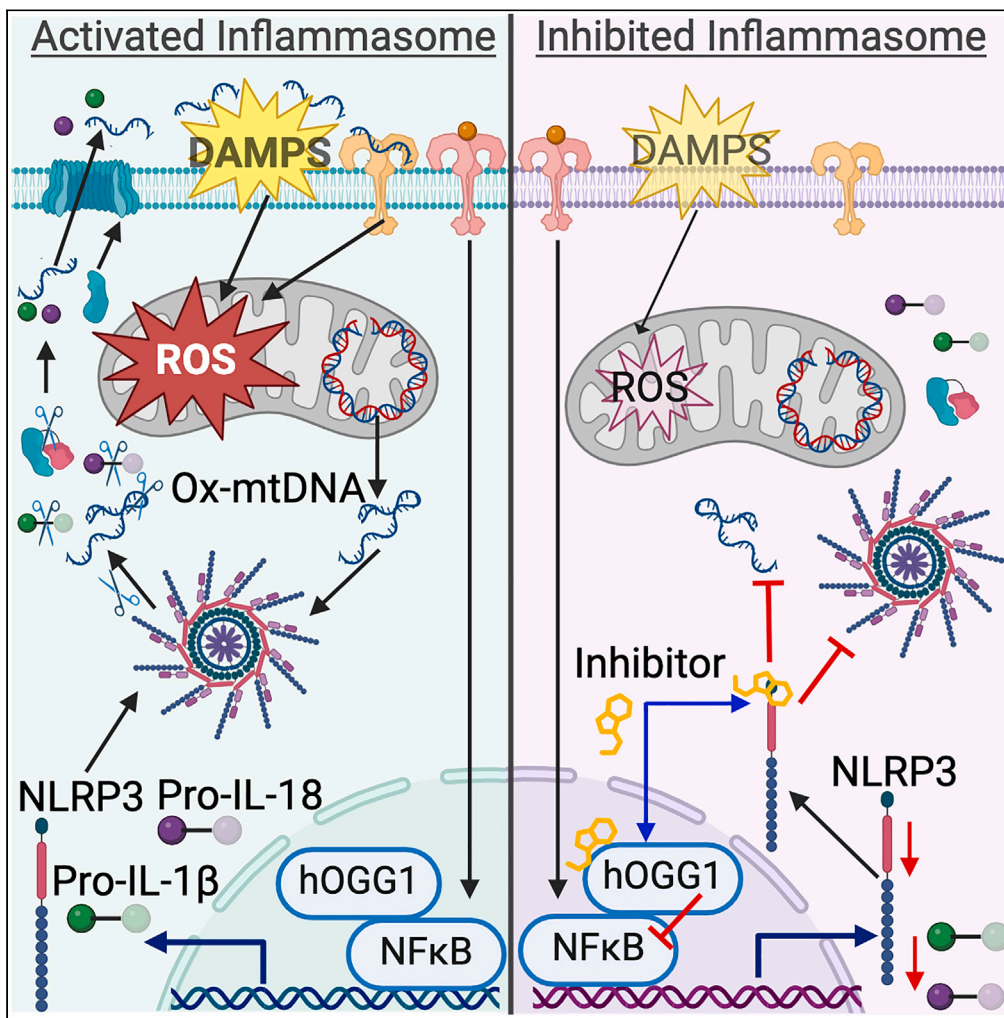NLRP3 plays a role in ox-
mtDNA release into the
cytosol

Article

Small molecule inhibitor binds to NOD-like receptor family pyrin domain containing 3 and prevents inflammasome activation

Angela Lackner,[1] Julia Elise Cabral,[1] Yanfei Qiu,[1] Haitian Zhou,[1] Lemuel Leonidas,[1] Minh Anh Pham,[1] Alijah Macapagal,[1] Sophia Lin,[1] Emy Armanus,[1] and Reginald McNulty[1,2,3,*]

SUMMARY

Despite recent advances in the mechanism of oxidized DNA activating NLRP3, the molecular mechanism and consequence of oxidized DNA associating with NLRP3 remains unknown. Cytosolic NLRP3 binds oxidized DNA which has been released from the mitochondria, which subsequently triggers inflammasome activation. Human glycosylase (hOGG1) repairs oxidized DNA damage which inhibits inflammasome activation. The fold of NLRP3 pyrin domain contains amino acids and a protein fold similar to hOGG1. Amino acids that enable hOGG1 to bind and cleave oxidized DNA are conserved in NLRP3. We found NLRP3 could bind and cleave oxidized guanine within mitochondrial DNA. The binding of oxidized DNA to NLRP3 was prevented by small molecule drugs which also inhibit hOGG1. These same drugs also inhibited inflammasome activation. Elucidating this mechanism will enable the design of drug memetics that treat inflammasome pathologies, illustrated herein by NLRP3 pyrin domain inhibitors which suppressed interleukin-1β (IL-1β) production in macrophages.

INTRODUCTION

Inflammation is the body's temporary response to resolve an infection. Prolonged and uncorrected infection results in an overstimulated innate immune system that can lead to septic shock, organ failure, fibrosis, and cancer. The NOD-like receptor family pyrin domain containing 3 (NLRP3) inflammasome is a key mediator of tissue damage and pathogen[1] or toxicant[2] infection. The pathogenic role of NLRP3 was first discovered in humans harboring gain of function disease mutants.[3] The NLRP3 inflammasome is a megadalton multi-protein complex consisting of NLRP3, ASC (apoptosis-associated speck-like protein containing a CARD (caspase activation and recruitment domain)),[4] pro-caspase-1, and NEK7 (Never in mitosis A (NIMA) – related kinase 7). Inflammasome autocleavage of pro-caspase-1 yields an active caspase-1 (p20/p10) heterotetramer. Caspase-1 protease activity leads to bioactive IL-1β, IL-18,[5] and cleavage of gasdermin D (GSDMD) at Asp275 which causes GSDMD to oligomerize and insert itself into the membrane. The electrostatic potential of its pore-lining residues allows selective transport of compatibly charged molecules, which include IL-1β, IL-18, ATP, inflammatory caspases, cleaved GSDMD, and other cytokines and chemokines.[6] These molecules amplify the immune response and recruit new immune cells that attempt to ameliorate the pathogen or danger signal. Extended efflux of molecules from macrophages causes a loss of cell membrane integrity, ultimately leading to cell death.

Canonical NLRP3 inflammasome activation consists of a 2-step activation process.[7] Transcriptional priming can occur through bacterial LPS binding to TLR2/4 receptor, which leads to NF-κB induced expression of NLRP3 inflammasome subunits, pro-IL-18, and pro-IL-1β.[8] Reactive oxygen species (ROS) production in the mitochondria results in cytidine/uridine monophosphate kinase 2 (CMPK2) causing mitochondrial transcription.[9] The unraveling of mtDNA required for transcription exposes the DNA to ROS which causes the oxidation of mitochondrial DNA.[10] Elimination of oxidized DNA by human 8-oxoguanine DNA glycosylase 1 (hOGG1) or mitophagy inhibits inflammasome activation.[11,12] The presence of foreign and cytosolic signals including alum, asbestos, SARS-CoV-2, or ATP overwhelm initial NLRP3 inhibition to promote inflammasome assembly and activation. The sustained presence of mitochondrial ROS during mitochondrial replication further exacerbates oxidized mitochondrial DNA (Ox-mtDNA). Ox-mtDNA is cleaved to 500–650 bp fragments by flap endonuclease 1 (FEN1), which allows Ox-mtDNA to be exported to the cytosol via mitochondrial permeability transition pores (mPTP) and voltage-dependent anion channels (VDAC) where it can associate with NLRP3 and promote assembly and activation.[13]

We have previously shown purified NLRP3 can directly bind Ox-mtDNA.[14] Furthermore, NLRP3 pyrin shares a similar protein fold with hOGG1, which suggests NLRP3 might have both glycosylase and nuclease activity similar to hOGG1. This study aims to capture if NLRP3 has glycosylase activity and if preventing such activity with small molecules affects inflammasome activation. We show herein that NLRP3

[1]Laboratory of Macromolecular Structure, Department of Molecular Biology and Biochemistry, Charlie Dunlop School of Biological Sciences, University of California, Irvine, Steinhaus Hall, Irvine, CA 92694-3900, USA
[2]Department of Pharmaceutical Sciences, University of California, Irvine, Steinhaus Hall, Irvine, CA 92694-3900, USA
[3]Lead contact
*Correspondence: rmcnulty@uci.edu
https://doi.org/10.1016/j.isci.2024.110459

Figure 1. NLRP3 Pyrin domain shares a similar fold with hOGG1 and cleaves Ox-mtDNA

(A) NLRP3$_{(1-93)}$ and hOGG1$_{(248-345)}$ sequence alignment and secondary structure depiction. Cyan asterisks mark residues shared between NLRP3 and hOGG1 that play a pivotal role in binding and DNA base excision in hOGG1.

(B) Biotinylated 90 base pair Ox-mtDNA incubated with NLRP3 pyrin and APE1, then probed with a streptavidin antibody shows DNA cleavage (green bracket). Schematic of single stranded oxDNA (blue) with the location of 8-oxo-dG's (G) shown below gel image.

(C) Western blot band quantification of oxDNA cleavage by NLRP3 pyrin with and without APE1. Error bars: mean $\pm$ SEM, analyzed with one-way ANOVA. PYD/APE1 with oxDNA N = 3, PYD with oxDNA N = 13. *p = 0.0311 ****p < 0.0001.

(D) Schematic of 90bp Ox-mtDNA used with multiple 8-oxodG's.

(E) NLRP3 pyrin domain (gray) structure residues 3–78 with helices labeled α1-α5. Superposition of hOGG1 (orange) bound to oxidized DNA shown with corresponding helices αL-αO residues 248–325.

(F) NLRP3 pyrin (PDBID: 7PZC, amino acids 1–91) contains a glycine/proline-rich region between amino acids 32 and 42, linking helices α2 and α3, and beginning with an aspartic acid (Asp31). NLRP3: gray, GPD-like loop: yellow.

(G) SWISS-MODEL projection of NLRP3 pyrin based on hOGG1 bound to Ox-DNA docked into the structure of hOGG1 bound to Ox-DNA (PDBID: 1EBM, amino acids 230–325). The GPD-like region of NLRP3 (amino acids 32–42) structurally aligns with a similar loop in hOGG1 (amino acids 279–291) which links helices αM and αN and also begins with an aspartic acid (Asp278). NLRP3: gray; hOGG1: orange.

can indeed cleave Ox-mtDNA. We also show small molecule drugs that prevent hOGG1 from interacting with oxidized DNA also prevent NLRP3 from interacting with Ox-mtDNA and block inflammasome activation in mouse macrophages.

RESULTS

NOD-like receptor family pyrin domain containing 3 pyrin cleaves oxidized DNA

The active site of hOGG1 has been well characterized with the location of amino acids that interact with oxidized DNA illustrated by the crystal structure.[15] Both sequence alignment and 3D superposition of hOGG1 and NLPR3 pyrin domain reveal a similar protein fold and many amino acids that are identical or similar.

Glycosylases are the first enzymes in base excision repair (BER) and can recognize and excise oxidized bases from DNA lesions. All glycosylases that remove oxidized bases also cleave DNA by nucleophilic attack on the DNA backbone, generating a Schiff base protein-DNA intermediate via a lyase reaction using the amine group of a conserved lysine, thereby acting bifunctionally.[16] This process results in cleavage of the N-glycosyl bond and release of the oxidized base, leaving an apurinic site (AP site) in the DNA which can be recognized by an AP endonuclease, APE1.[17] APE1 creates a nick in the 5' end of the AP site and adds a 3'-OH which is required for DNA polymerase to add a new replacement base.[18]

Since the fold and sequence of NLRP3 and hOGG1 are similar and NLRP3 pyrin can directly bind oxidized DNA (Figures 1A–1G),[14] we probed if NLRP3 pyrin domain could cleave oxidized DNA. NLRP3 pyrin incubated with 90-mer single stranded Ox-mtDNA containing several oxidized guanines produced cleavage products that migrated lower than DNA alone (Figure 1B). The cleavage product was enhanced upon the addition of APE1, which recognized the apurinic sites created by NLRP3 pyrin. The cleavage bands of the 8-oxo-dG-containing DNA sequence were plotted and quantified using a one-way ANOVA (Figures 1C and 1D). The oxDNA band intensity increased when incubated with either APE1 or the pyrin domain, or with both. This elevation is attributed to the stability of the G-quadruplex in the DNA and subsequent availability of the biotin tag (Figure S1).[19] This data shows NLRP3 pyrin could behave like a bifunctional glycosylase; able to remove the oxidized base and cleave the backbone.

To determine if the activity was specific to the pyrin domain of NLRP3, we performed the same assay with the NLRP3 NACHT-LRR$_{(94-1034)}$ construct, which lacks the pyrin domain. With increasing concentrations of protein incubated with 90-mer single stranded Ox-mtDNA cleavage was not seen, indicating that DNA cleavage is specific to the pyrin domain (Figure S2).

NOD-like receptor family pyrin domain containing 3 and human glycosylase share protein fold features

Sequence comparison for NLRP3$_{(1-80)}$ pyrin domain and hOGG1$_{(248-326)}$ showed many residues that are either the same or similar between the two proteins. The sequence identity and similarity were 31.3% and 45.5%, respectively (Figure S3). Due to the moderate similarity in sequence, we compared the relative position of secondary structure in 3D (protein fold) of NLRP3 pyrin to hOGG1 (Figure 1E). We first superposed PDB: 7PZC NLRP3 pyrin$_{(1-81)}$ and PDB: IEBM hOGG1$_{(248-326)}$.[20] To evaluate protein fold, the relative positions of NLRP3 pyrin helices α1-α5 was compared to corresponding positions of helices αL-αO for hOGG1 in the oxidized DNA-bound state (Figure 1E) and the DNA-free state (Figure S4). We note NLRP3's α3 is a very short stretch from residues 42–49 which accounts for the extra helix topology. Helices α1 and αL did not align. The hOGG1 structure has a disordered stretch in the equivalent space of NLRP3 helix$_{α1}$. The similarities between these two N-terminal locations include they are both predicted to be intrinsically disordered regions (IDR's), which are regions predicted to convert between ordered and disordered (Figure S5).[21] NLRP3$_{α2(17-31)}$ and hOGG1$_{αM(268-280)}$ traverse the same direction with different angles and have similar lengths of 19 Å and 17 Å, respectively. After the second helix, there is a loop for both proteins but in opposite directions. The NLRP3 loop (31–42) and hOGG1 loop (280–293) are similar in size, but the hOGG1 loop is slightly longer. Along the direction of the hOGG1 loop, NLRP3's loop has a small helix, helix$_{α3(42-49)}$, which has a strong kink (Ala49 to Asp50) causing a change in direction to continue along the same path as hOGG1$_{αN}$. NLRP3$_{α3}$ traverses the same direction as the hOGG1 loop. Interestingly, both of the proteins have an IDR signature[21] for this region suggesting they are prone to convert between ordered and disordered secondary structures (Figure S5) according to the Database of Disordered Protein Predictions (D2P2).[22] The break in NLRP3$_{α3(42-49)}$ directly connects to NLRP3$_{α4}$, which aligns with hOGG1$_{αN}$.
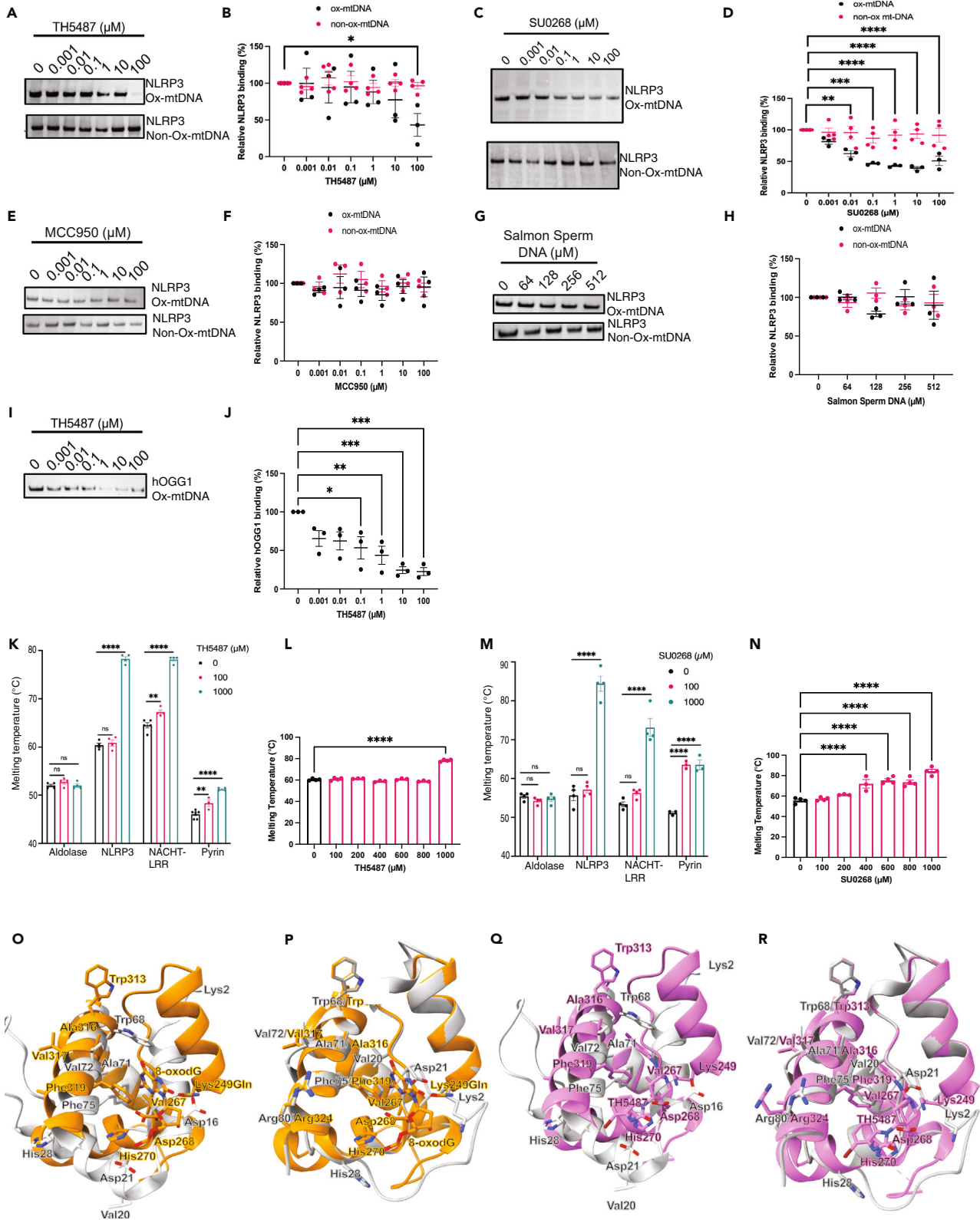
Figure 2. hOGG1 inhibitors bind NLRP3 and inhibit binding to Ox-mtDNA

(A) An anti-NLRP3 Western blot on the bound fraction of NLRP3 to Ox- and non-Ox-mtDNA in the presence of TH5487 inhibitor from 0.001 to 100 μM.

(B) Quantification of (A) shown as relative band intensity, $N = 4$, Error bars: mean $\pm$ SEM, analysis by one-way ANOVA, $*p = 0.0179$.

(C) An anti-NLRP3 Western blot on the bound fraction of NLRP3 to Ox- and non-Ox-mtDNA in the presence of SU0268 inhibitor from 0.001 to 100 μM.

(D) Quantification of (C) shown as relative band intensity $N = 4$, Error bars: mean $\pm$ SEM, analysis by one-way ANOVA, $**p = 0.0069$, $***p < 0.0005$, $****p < 0.0001$.

(E) An anti-NLRP3 Western blot on the bound fraction of NLRP3 to Ox- and non-Ox-mtDNA in the presence of MCC950 inhibitor from 0 to 100 μM.

(F) Quantification of (E) shown as relative band intensity, $N = 3$.

(G) An anti-NLRP3 Western blot on the bound fraction of NLRP3 to Ox- and non-Ox-mtDNA in the presence of Salmon Sperm DNA from 0 to 512 μM.

(H) Quantification of (G) shown as relative band intensity, $N = 3$.

(I) An anti-hOGG1 Western blot on the bound fraction of hOGG1 to Ox- and non-Ox-mtDNA in the presence of TH5487 inhibitor from 0.001 to 100 μM μM.

(J) Quantification of (I) shown as relative band intensity, $N = 3$, Error bars: mean $\pm$ SEM, analysis by one-way ANOVA, $*p = 0.0069$, $**p = 0.0004$, $***p < 0.0001$.

(K) Melting temperature data in the presence of TH5487. $N = 4$–8, Error bars: mean $\pm$ SEM, analysis by one-way ANOVA, NACHT-LRR $**p = 0.0015$. pyrin $**p = 0.0036$, $****p < 0.0001$.

(L) Melting temperature data in the presence of TH5487 at an expanded dose range from 100 to 1000 μM. $N = 4$–8, Error bars: mean $\pm$ SEM, analysis by one-way ANOVA, $****p < 0.0001$.

(M) Melting temperature data in the presence of SU0268. $N = 4$ Error bars: mean $\pm$ SEM, analysis by one-way ANOVA, $P****<0.0001$.

(N) Melting temperature data in the presence of SU0268 at an expanded dose range from 100 to 1000 μM $N = 3$. Error bars: mean $\pm$ SEM, analysis by one-way ANOVA, $P****<0.0001$.

(O) NLRP3 pyrin (gray) PDBID: 7PZC docked into the structure of hOGG1 bound to Ox-DNA (orange) PDBID: 1EBM.

(P) SWISS-MODEL generated NLRP3 pyrin bound to Ox-DNA (gray) docked into the structure of hOGG1 bound to Ox-DNA PDBID: 1EBM.

(Q) NLRP3 pyrin PDBID: 7PZC docked into the structure of hOGG1 bound to TH5487 (pink) PDBID: 6RLW.

(R) SWISS-MODEL projection of NLRP3 pyrin based on hOGG1 bound to Ox-DNA docked into the structure of hOGG1 bound to TH5487 (PDBID: 6RLW).

Both proteins then turn to form NLRP3$_{\alpha5(63-78)}$ and hOGG1$_{\alpha O(310-326)}$ with those helices also aligned but slightly out of phase. This forms the end of the hOGG1 C-terminus while the NLRP3 pyrin domain has an additional helix, NLRP3$_{\alpha6(80-90)}$.

Human glycosylase OGG1 contains a Helix-hairpin-Helix (HhH) motif followed by a GPD region, a Gly/Pro-rich region which terminates with an Asp.[23] The GPD loop in hOGG1 is critical for the cleavage of oxidized DNA.[15] Changing the conserved Asp268 to Asn268 is a loss of function mutation for hOGG1.[24] In our sequence alignment, NLRP3 Asp21 has an identity to hOGG1Asp268 (Figure 1A). However, NLRP3 Asp21 is not preceded by an HhH domain. Interestingly, NLRP3's pyrin domain contains an HhH motif formed with a hairpin between helices α2- α3 (Figure 1F). The 12-residue hairpin is GP-rich beginning with Asp31, Pro33, Pro34, Lys36 (apex), Gly37, Pro40, and Pro42. Unlike hOGG1 which has a GP-rich motif terminating with Asp268, NLRP3's GP-rich hairpin begins with Asp31. Interestingly, this second GPD-like region that starts with Asp also maps to sequence alignment with hOGG1 residues 278–291 (Figure 1A). In hOGG1, the equivalent region is about 180° opposite the HhH motif. Similar to the HhH, this loop makes critical contacts with DNA which include Ala288[25] which, when mutated, can decrease substrate binding up to 60%.[26] We generated a model of NLRP3 pyrin bound to oxidized DNA using SWISS-MODEL.[27] The NLRP3 pyrin GPD-like region 31–42 traverses the same direction and orientation as hOGG1 278–291, in which both proteins start with Asp (Figure 1G), confirming this region has the propensity to interact with DNA.

Glycosylase inhibitors prevent NOD-like receptor family pyrin domain containing 3 binding to oxidized DNA

It has been reported that NLRP3 can interact with oxidized DNA.[13,14,28] The inhibitor TH5487 binds the 8-oxodG binding site of hOGG1 to prevent binding to oxidized DNA.[29] Since the fold of NLRP3 and hOGG1 are similar, we probed if TH5487 could prevent NLRP3 pyrin from recognizing Ox-mtDNA. We found a concentration-dependent inhibition of NLRP3 binding to Ox-mtDNA in the presence of TH5487 where binding was inhibited with 100 μM TH5487 (Figures 2A and 2B). No significant loss of binding to non-oxidized DNA was observed in the presence of the drug. We also tested the hOGG1 inhibitor SU0268[30] and saw a similar trend, in which the drug showed a concentration-dependent inhibition of NLRP3 binding to Ox-mtDNA ranging from 0.01 μM to 100 μM, but did not affect binding to non-oxidized DNA (Figures 2C and 2D). We also examined if MCC950, a drug known to bind the NACHT domain and inhibit activation, could prevent NLRP3's interaction with Ox-mtDNA. However, our experiments showed no significant difference in NLRP3 binding to either Ox-mtDNA or non-oxidized mtDNA in the presence of MCC950 (Figures 2E and 2F). Similarly, salmon sperm DNA did not affect the binding of NLRP3 to non-oxidized mtDNA or Ox-mtDNA (Figures 2G and 2H), showing that NLRP3 has a preference for mtDNA. Collectively, these results suggest that drugs targeting the NLRP3 pyrin domain inhibit interaction with Ox-mtDNA. To validate our assay, we used hOGG1 as a positive control, observing inhibited binding to Ox-mtDNA in a dose-dependent manner with as low as 0.1μM TH5487 (Figures 2I and 2J).

Glycosylase inhibitors directly bind NOD-like receptor family pyrin domain containing 3

To examine if TH5487 could directly bind NLRP3, we performed a thermal shift assay. The average melting temperature (T_m) of full-length NLRP3 shifted from an average value of 60.4°C–78.3°C with 1 mM TH5487 indicating the drug had directly bound to NLRP3 and delayed the T_m by an increase of 17.9°C (Figures 2K and 2L). We repeated this assay with the pyrin NLRP3$_{(1-93)}$ and the NACHT-LRR NLRP3$_{(94-1034)}$ domains. We found the pyrin domain could bind TH5487 as evidenced by the increase in T_m from 46.1°C to 48.3°C and 51.3°C with 100 μM and 1 mM TH5487, respectively. Interestingly, the NACHT-LRR construct was also able to bind TH5487 and provide even more protein stability. The T_m was increased from 64.4°C to 67.2°C and 78.1°C with 100 μM and 1 mM TH5487, respectively (Figure 2K). Similar results were seen for drug SU0268 which had an increased T_m of 72°C at 400 μM for full-length NLRP3 and an increased T_m of 63.5°C at 100 μM for pyrin NLRP3$_{(1-93)}$ (Figures 2M and 2N). As a

control, we tested if the protein aldolase conferred similar changes to T_m in the context of both drugs. In these experiments, neither 100 μM nor 1 mM TH5487 or SU0268 caused a significant difference in the T_m of aldolase compared to protein alone (Figures 2K and 2M).

NOD-like receptor family pyrin domain containing 3 and human glycosylase share active site residues

Superposition of NLRP3 pyrin$_{(1-81)}$ with hOGG1$_{(248-326)}$ shows that many of the amino acids important in hOGG1 binding oxidized DNA (Figure 1C) are also found in the active site for the 8-oxodG and the TH5487-bound states (Figures 2O–2R; Table S1). The RMSD between NLRP3 pyrin and hOGG1 between 17 pruned atom pairs was 1.147 Å. Major differences appeared at the beginning of each model where the alpha carbon (Cα) for the critical Lys2 was 13.1 Å away from the corresponding residue Lys249 in hOGG1. Other amino acids in helices α3 – Leu54/299 and α4 - Trp 68/313, were separated by 0.6 and 3.8 Å, respectively. So, although many residues were in the same vicinity, deviations were large enough to suggest NLRP3 pyrin would undergo a conformation change upon binding oxidized DNA. To generate a homology model of NLRP3 pyrin bound to oxidized DNA, we used the NLRP3$_{1-85}$ sequence and hOGG1$_{248-326}$ (PDBID: 1EBM) with the SWISS-MODEL software. A single model was generated with a MolProbity score of 1.78 and a Ramachandran favored percentage of 94.87% (Table S2). The model illustrates a rearrangement of NLRP3 helix α1. The Lys2/249 distance decreased from 13.16 Å to 0.124 Å. Many residues including Ala4, Cys8, and Ala11 of NLRP3 all decreased to less than 1 Å apart in the NLRP3 model (Table S3). All amino acids do not completely move to the same location. For example, Asp21/268 decreased from 7.551 Å to 6.322 Å apart. The corresponding to residues of NLRP3 in the active site of hOGG1 are Gln45/294, Trp68/313, Ala69/314, Ala71/316, Val72/317, Phe75/319, Ala77/321, Arg80/324, respectively. These residues all moved from an initial Cα-Cα distance of 2–20 Å to less than 1 Å apart.

Gain of function mutant has enhanced oxidized mitochondrial DNA cleaving ability

hOGG1 interacts with 8-oxodG in DNA through critical contacts made by Lys249 and Asp268, which are essential for base excision. Unlike hOGG1, NLRP3 features additional Lys/Asp residues near the active site, potentially offering compensatory redundancy for interaction with 8-oxo-dG. Given this redundancy, creating an ideal loss-of-function mutant in NLRP3 would likely require mutating several residues, which might destabilize the overall structure of the pyrin domain. Consequently, we pursued an alternative strategy by using our model to predict a gain-of-function mutation. The electrostatic surface potential near the active site of the pyrin domain is predominantly negative, leading us to hypothesize that neutralizing this charge could enhance catalytic activity with negatively charged Ox-mtDNA (Figure S6). Building on our previous findings, we identified that the gain-of-function NLRP3 D21H mutation, which corresponds to Asp268 in hOGG1, might also enhance interaction with oxidized mtDNA. Notably, this mutation also causes the autosomal dominant autoinflammatory disease CAPS phenotype.[31] We employed fluorescence polarization (FP) to quantify DNA cleavage; an increase in FP signal indicates increased binding, whereas a decrease suggests DNA cleavage (Figure 3A). Full-length NLRP3 demonstrated cleavage capability, as indicated by a 45% reduction in FP signal at a concentration of approximately 62.5 μg/mL, confirming that full-length NLRP3 can cleave Ox-mtDNA, similar to isolated PYD in the gel-based assay (Figure 3B). In the FP assay, we tested a control protein, aldolase, and did not see any change in the FP signal (Figure 3C) suggesting that the observed cleavage of Ox-mtDNA is NLRP3 specific. Notably, the D21H mutant of full-length NLRP3 showed an 84% reduction in FP signal at 62.5 μg/mL, indicating a significantly enhanced cleavage ability compared to the wild type (Figure 3D). Given our earlier findings that TH5487 and SU0268 inhibit NLRP3's binding to oxidized DNA, we tested whether these inhibitors could also block the enhanced cleavage by NLRP3 D21H. Increasing concentrations of these drugs demonstrated the dose-dependent inhibition of cleavage. At 10 μM, both TH5487 and SU0268 effectively prevented cleavage, with FP signals comparable to those observed with DNA alone (Figure 3E).

Macrophages display NOD-like receptor family pyrin domain containing 3 dependent oxidized mitochondrial DNA cleavage

To investigate whether Ox-mtDNA cleavage is dependent on NLRP3 within cells, we analyzed DNA in the mitochondria and cytoplasm of primed and activated immortalized bone marrow-derived macrophages (iBMDMs). We observed DNA near 16 kB in the mitochondria and cleaved species around 1 kB in the cytoplasm, consistent with the approximate size of D loop mtDNA. Additionally, a smaller cleaved species approximately 600 bp was detected in the cytosol (Figures 4A and S7). These cleaved species were not present in the cytosol of NLRP3 knockout (KO) iBMDMs (Figure 4B), indicating a role for NLRP3 in their formation. We further confirmed that the DNA detected in the cytoplasm was indeed D loop mtDNA by running a PCR with primers specific to a 591 bp fragment of the D loop mtDNA. This fragment was found in both the mitochondria and the cytosol, whereas a larger 5698 bp mtDNA fragment was only detected in the mitochondria (Figure 4C).

Blocking NOD-like receptor family pyrin domain containing 3 binding to oxidized DNA prevents inflammasome activation

It was previously demonstrated that targeting OGG1 to the mitochondria would decrease IL-1β production.[13] Moreover, the ablation of OGG1 leads to an increase of IL-1β since oxidized mtDNA has not been repaired.[13] So, inhibiting OGG1 with TH5487, should cause an increase in IL-1β. Given we already observed that TH5487 could bind NLRP3, we examined what would happen to IL-1β in the presence of TH5487 under conditions that should promote inflammasome activation. Interestingly, we found that the stimulation of NLRP3 inflammasome activation with LPS/ATP in the presence of TH5487 caused a decrease in IL-1β production with concentrations from 0.01 to 100 μM (Figures 5A, 5B, S8A, and S8B). Lower concentrations of TH5487 also decreased the amount of cleaved caspase-1 in the supernatant and increased pro-caspase-1 in macrophages, which is consistent with a decrease in NLRP3 activation (Figures 5A and S9). The hOGG1 inhibitor, SU0268, showed the same significant decrease in NLRP3-dependent IL-1β release, as well as a decrease in secreted caspase-1, and TNF-α as well as pro-IL-1β in the lystate. (Figures 5C, 5D, S8C, S8D, and S10).
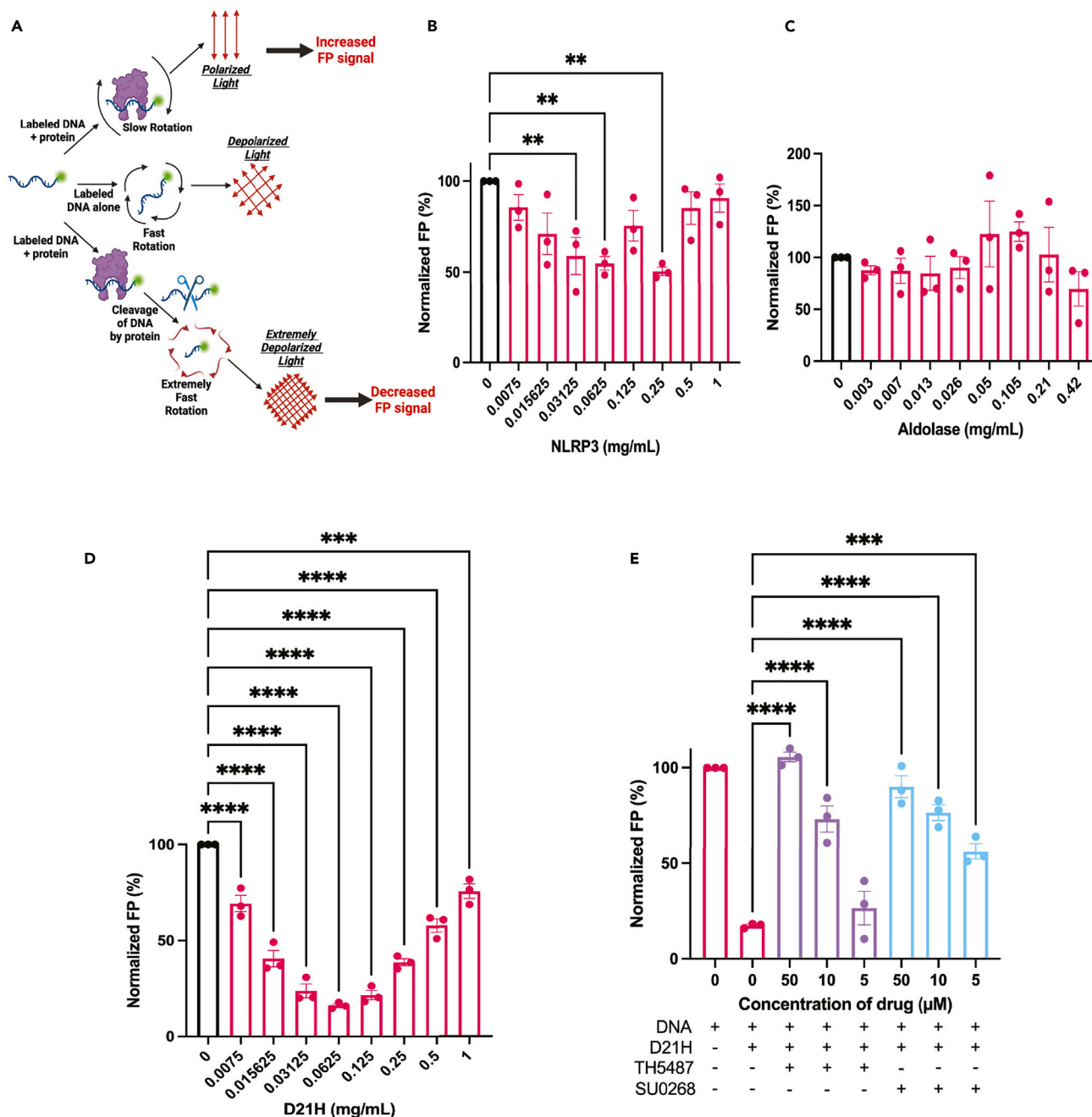
Figure 3. NLRP3 mutant D21H cleave ox-mtDNA more readily than wild-type NLRP3 and this interaction can be inhibited by hOGG1 inhibitors TH5487 and SU0268

(A) Simplified schematic of fluorescence polarization workflow. Wild-type NLRP3 (B) D21H NLRP3 (C) and aldolase (D) at varying concentrations were incubated with 100 μM of Cy5-labeled 20 bp ox-mtDNA and the amount of DNA cleavage was quantified the relative percent of the FP signal compared to DNA alone. (E) 0.0625 mg/mL of D21H mutant was pre-incubated with both hOGG1 inhibitors at doses from 5 to 50 μM then proteins were incubated with 100 μM of Cy5-labeled 20 bp Ox-mtDNA. The amount of cleavage was quantified by a loss in OD450 signal as quantified by fluorescence polarization and normalized to the DNA alone signal. For all graphs, error bars: mean ± SEM, $N = 3$, ****$p < 0.0001$, ***$p < 0.0002$, **$p < 0.0054$. Analyzed by one-way ANOVA.

Blocking inflammasome activation prevents the secretion of oxidized mitochondrial DNA

We hypothesized that preventing NLRP3 from interacting with Ox-mtDNA would inhibit its ability to cleave DNA in the cytosol of macrophages, resulting in the detection of larger DNA fragments in the cytosol. Contrary to our expectations, we observed that treatment with TH5487 or SU0268 not only eliminated the presence of D loop mtDNA in the cytosol (Figure 4C), but also prevented the secretion of
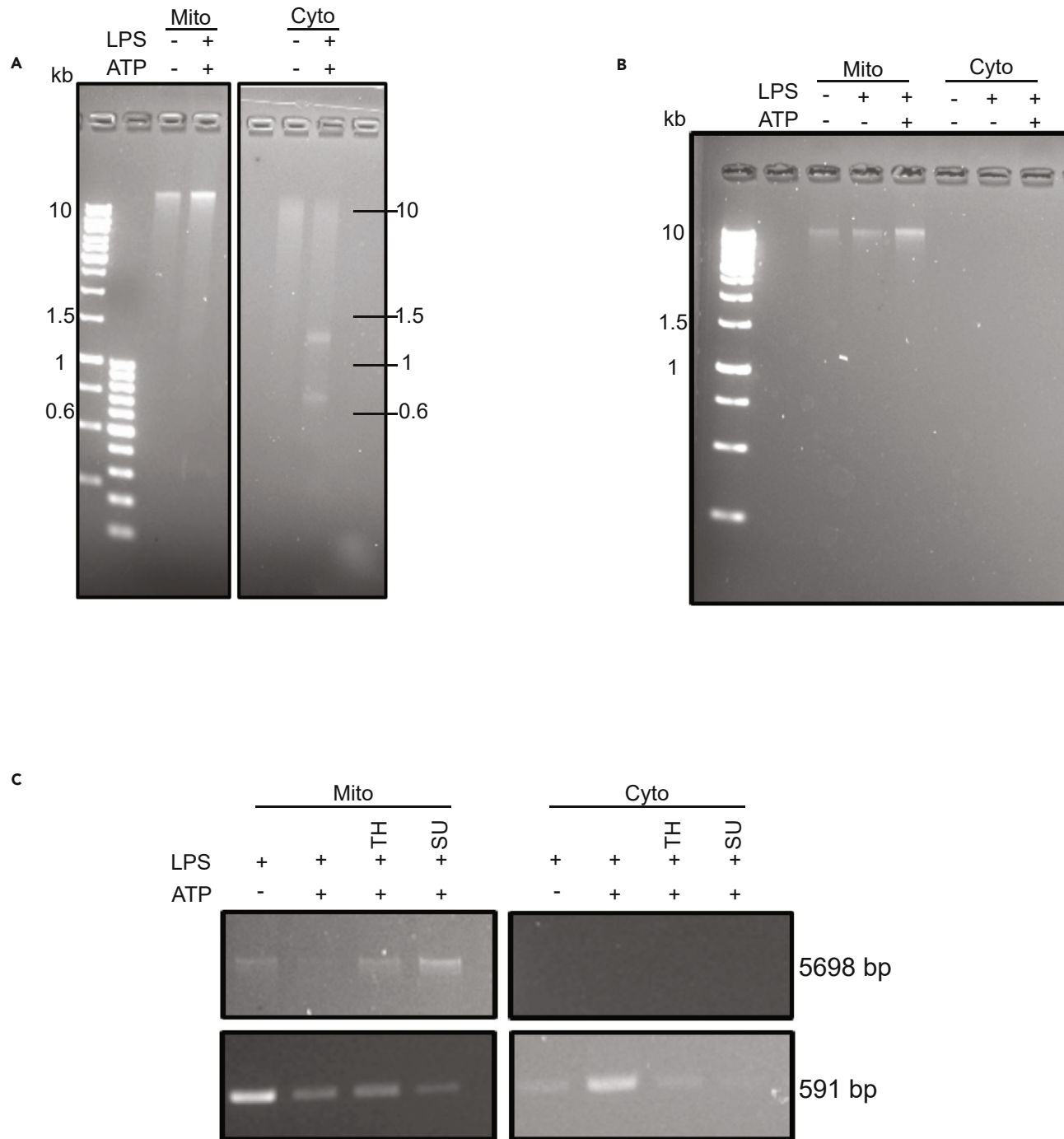
Figure 4. mitochondrial DNA is cleaved and secreted into the cytosol in an NLRP3-dependent manner which can be inhibited by hOGG1 inhibitors TH5487 and SU0268

(A) DNA isolated from the mitochondria or cytosol of inflammasome-activated immortalized mouse BMDMs and ran on a 2% agarose gel.

(B) DNA isolated from either the mitochondria or cytosol of inflammasome activated NLRP3 knockout immortalized mouse BMDMs and run on a 2% agarose gel.

(C) DNA isolated from either the mitochondria of cytosol of inflammasome-activated immortalized mouse BMDMs was amplified by primers targeting a larger fragment of mitochondrial DNA (5698 bp) or a smaller fragment of mitochondrial DNA (591 bp) and run on a 2% agarose gel.
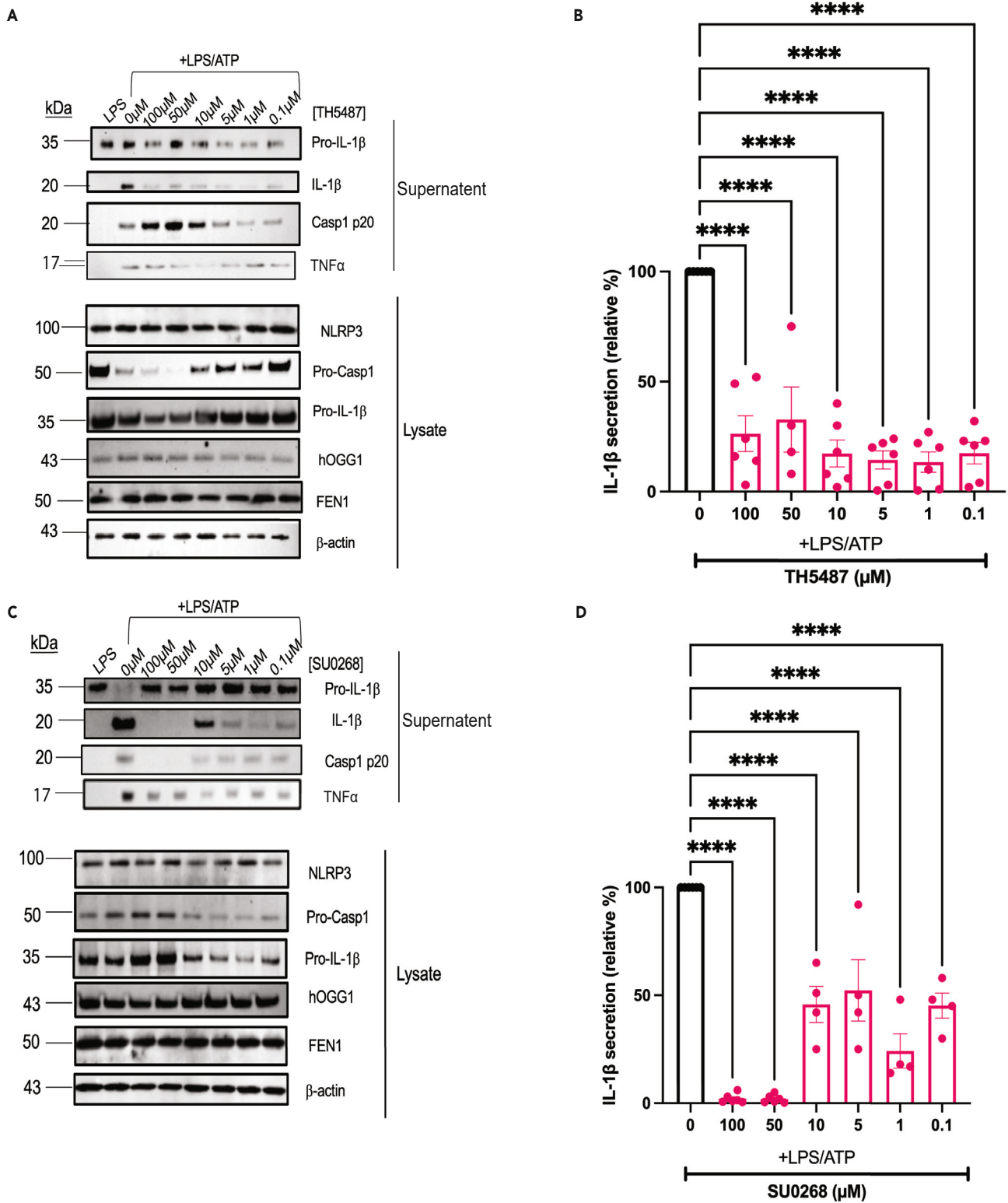
Figure 5. hOGG1 inhibitors TH5487 and SU0268 inhibit IL-1β secretion

(A) Representative western blots of inflammasome-related proteins in LPS/ATP treated or untreated immortalized mouse macrophages challenged with 0–100 μM TH5487.

Figure 5. Continued

(B) Quantified relative amount of IL-1β in the supernatant of LPS/ATP stimulated immortalized mouse macrophages challenged with 0–100 μM TH5487. Error bars: mean ± SEM, analyzed with one-way ANOVA. $N = 6$, ****$p < 0.0001$.

(C) Representative western blots of inflammasome-related proteins in LPS/ATP treated or untreated immortalized mouse macrophages challenged with 0–100 μM SU0268.

(D) Quantified relative amount of IL-1β in the supernatant of LPS/ATP stimulated immortalized mouse macrophages challenged with 0–100 μM SU0268. $N = 4–6$ Error bars: mean ± SEM, analyzed with one-way ANOVA. ****$p < 0.0001$.

Ox-mtDNA from the cells (Figures 6A and 6B) as confirmed by 8-oxodG ELISA on the supernatant of iBMDMs. The well-characterized NLRP3 inhibitor, MCC950, was also tested and showed similar inhibition (Figure 6C). This aligns with the role of all three of these drugs in inhibiting inflammasome activation and pyroptosis. To investigate the levels of Ox-mtDNA inside the cell, 8-oxo-dG ELISAs were run on the cytosolic and mitochondrial fractions of iBMDMs (Figures 6D and 6E). All three drugs decreased the amount of cytosolic Ox-mtDNA in wild-type cells, where a decrease in cytosolic Ox-mtDNA was not observed in NLRP3 knockout (KO) macrophages, confirming that this response is NLRP3-dependent (Figure 6D). This notable decrease in cytosolic Ox-mtDNA occurred with as little as 1 μM MCC950, 0.1 μM TH5487, and 5 μM SU0268. Although a similar decrease was noted in the mitochondria, there was no significant difference between wild-type (WT) and NLRP3 KO macrophages, despite observable reductions in both (Figure 6E). To confirm that the changes in mtDNA levels in the cytosol were not due to a loss in overall mtDNA amounts, we ran qPCR experiments on the cytosolic and mitochondrial fractions of iBMDM cells and observed the relative amounts of D loop and Cox1 mtDNA levels in the cytosol normalized to the mitochondrial levels (Figures 6F and 6G).[9,32] In both cases, the relative amounts of cytosolic mt-DNA were increased by NLRP3-activated iBMDMs, and this increase was significantly inhibited by treatment with TH5487, SU0268, or MCC950 at 10 μM. There was no significant difference between wild type and NLRP3 KO iBMDM's in cytosolic D loop level in the presence of LPS alone. Cytosolic D loop mtDNA increased in WT, but not NLRP3 KO macrophages upon inducing activation with LPS/ATP (Figure 6F). Our inability to detect cytosolic mtDNA in NLRP3 KO iBMDM's suggests NLRP3 may play a direct role in Ox-mtDNA release from the mitochondria.

DISCUSSION

A connection between NLRP3 and Ox-mtDNA has been reported, however, the direct consequence and mechanism of NLRP3 binding Ox-mtDNA has not been established. Herein we show that NLRP3 pyrin can excise oxidized guanine and subsequently cleave Ox-mtDNA. Apurinic sites created by NLRP3 pyrin enable additional cleavage of Ox-mtDNA by APE1. We describe the similarities in sequence, protein fold, and 3D structure with that of human glycosylase hOGG1, which functions in BER to remove oxidized guanine. The structure of hOGG1 and NLRP3 pyrin are similar enough such that small molecules that inhibit hOGG1 can also inhibit NLRP3 inflammasome activation in macrophages stimulated with LPS/ATP. Here, we present a model of NLRP3 bound to oxidized DNA and to two small molecule inhibitors, TH5487 and SU0268. Our model of NLRP3 cleaving oxidized DNA is consistent with major amino acids known to participate in DNA catalysis based on hOGG1 superposition and sequence alignment including Lys2 and Asp21, equivalent to hOGG1 Lys249 and Asp268, respectively (Figure 1). The ability of NLRP3 pyrin to not only excise the base and create an AP site, but cleave the N-glycosyl backbone suggests NLRP3 has bifunctional glycosylase activity.

Small molecules that inhibit the glycosylase's ability to cleave oxidized DNA not only bind to NLRP3, but prevent NLRP3's interaction with Ox-mtDNA (Figures 2A–2F) and decrease NLRP3 inflammasome activation (Figure 5). Since OGG1 ablation increases NLRP3 activation,[13] use of these small molecule inhibitors to block NLRP3 activation may represent approaches to treat a variety of diseases for which NLRP3 inflammasome contributes, including metabolic dysfunction-associated fatty liver disease (MAFLD),[33] hepatocellular carcinoma (HCC),[34] rheumatoid arthritis,[35] keratitis,[36] and over-active NLRP3 found in patients with cryopyrin-associated periodic syndrome (CAPS).[3]

NLRP3 and hOGG1 have regions predicted to be intrinsically disordered, which by definition, maintain the ability to convert between order and disorder depending on presence of binding partners. Using the sequence of the pyrin domain with AlphaFold2, which is documented to perform poorly with IDP's, yields a structure that exactly matches the pyrin domain since that structure is readily available in the Protein Data Bank.[37] We found that SWISS-MODEL could produce a model that closely resembled hOGG1, which took into consideration not only sequence similarity, but order and disorder found in hOGG1 and the location of those residues in 3D. The superposition of NLRP3 pyrin with hOGG1 already shows several amino acids in NLRP3 that localize in the active site of hOGG1 in the proper vicinity to interact with oxidized DNA. The SWISS-MODEL generated structure of NLRP3, which represents the state of NLRP3 bound to oxidized DNA, not only has better superposition of amino acids in the active site, but the critical Lys2 needed to form nucleophilic attack and cleave oxidized DNA more closely matches the hOGG1 structure. This change is enabled by a rearrangement of NLRP3$_{α1}$ which has the propensity to stretch by unraveling α1-α2 transition (Figures 2O–2R and S4).

In our studies, we observed that NLRP3 inhibitors lead to a decrease in cytosolic mt-OxDNA. The reduction in cytosolic Ox-mtDNA could be mediated by the dual inhibition of hOGG1, which blocks the activation of NF-κB, thereby preventing the expression of priming inflammasome signals including pro-IL-1β. This inhibition would curtail the release of IL-1β and Ox-mtDNA via gasdermin D. Normally, extracellular Ox-mtDNA would initiate a robust TLR9-mediated response as a damage-associated molecular pattern (DAMP), initiating further signaling involving TNF-α and additional Ox-mtDNA, which in turn promotes more robust inflammasome activation. The absence of cytosolic Ox-mtDNA in the presence of these inhibitors suggests a crucial role for both priming and extracellular DAMP stimulation in driving a robust inflammasome response.

Figure 6. hOGG1 drugs TH5487 and SU0268 reduce the amount of 8-oxo-dG in the supernatant, cytosol, and mitochondria of inflammasome-activated immortalized mouse BMDMs

The supernatant of cells treated with varying doses of either TH5487 (A) SU0268 (B) or MCC950 (C) ranging from 0.0001 to 100 μM evaluated using an ELISA against 8-oxo-dG. Error bars are mean $\pm$ SEM, N = 3, Analyzed by one-way ANOVA, ****p < 0.0001, ***p = 0.0005, **p = 0.0041, *p = 0.0104. Purified DNA from the cytosol (D) or mitochondria (E) of cells treated with varying doses of TH5487, SU0268, or MCC950 ranging from 0.1 to 50 μM was evaluated using an ELISA against 8-oxo-dG. Error bars are mean $\pm$ SEM, N = 3, analyzed by two-way ANOVA, ***p = 0.0008, **p = 0.0012, *p = 0.0116.

(F) qPCR was run on purified DNA from the cytosol and whole cell fraction of inflammasome-activated wild type or NLRP3 knockout iBMDMs in the presence or absence of inhibitors and the normalized amounts of D loop mtDNA were quantified and analyzed by two-way ANOVA. Error bars are mean $\pm$ SEM, N = 3, *p = 0.0185, ***p < 0.0007 ****p < 0.0001 (G) qPCR was run on purified DNA from the cytosol and mitochondrial fraction of inflammasome-activated wild type iBMDMs in the presence or absence of inhibitors and the normalized amounts of mCox1 mtDNA were quantified and analyzed by one-way ANOVA. Error bars are mean $\pm$ SEM, N = 3, **p < 0.007.

It is quite interesting that the extramitochondrial presence of Ox-mtDNA, but not nuclear DNA, can induce arthritis when injected into mice.[38] Mitochondrial DNA is normally well protected via TFAM packaging into nucleoids,[39] however, mtDNA is exposed during CMPK-dependent mitochondrial replication which allows easy oxidation of D loop mtDNA. The nuclease FEN1 cleaves Ox-mtDNA into smaller fragments which can the exit the mitochondria via mPTP and VDAC channels.[13] Once in the cytoplasm, the oxidized DNA has been demonstrated to bind to cyclic GMP-AMP synthase (cGAS) when present in large amounts.[40–42] The cGAS-STING activation may synergize with the activation of NLRP3 inflammasome and the production of IL-1β and IL-18. Cytosolic DNA will eventually be expelled from the cell via gasdermin D-mediated pyroptosis. The released D loop Ox-mtDNA, which is rich in cytosine-phosphate-guanine (CpG) motifs, could then cause increased pro-inflammatory signaling as a DAMP by binding to the transmembrane protein TLR9 that leads to NF-κB signaling and IRF7-mediated type I IFN-β.[43] The preference for TLR9 interacting with oxidized DNA over non-oxidized DNA establishes a more robust TNF and IL-8 response.[44] The ability of NLRP3 to interact and remove oxidized guanine from oxidized DNA may serve to reduce inflammatory signaling similar to hOGG1. But clearly, situations that overwhelm the cell with cytosolic Ox-mtDNA cause inflammasome activation.[32] In this study, we focused on single-stranded Ox-mtDNA due to its relevance during mitochondrial DNA replication and transcription, where the D loop region is transiently exposed and susceptible to actions by enzymes such as FEN1. hOGG1 exhibits bifunctional glycosylase activity on double-stranded Ox-DNA and likely utilizes the cytosine opposite 8-oxo-dG to facilitate accurate base repair. Given that DNA repair in the cytosol is unfeasible, it makes sense that cytosolic NLRP3 responds to single-stranded Ox-DNA. This interaction not only potentially mitigates the severity of TLR9 activation but may also serve a structural role. Cytosolic Ox-mtDNA may directly contribute to NLRP3 inflammasome formation by binding to the pyrin domain. This interaction could facilitate the release of pyrin-pyrin interactions within the decameric core that stabilize the inactive oligomer,[45] thereby allowing a thermodynamically favored rearrangement to an active conformation capable of binding ASC.[4] Such a mechanism of activation could be enabled by 8-oxo-dG in mtDNA, 8-oxo-dG nucleosides, or other small molecules that bind at or near the pyrin domain, including PI4P.[46] Future work will involve probing the molecular determinants of NLRP3–Ox-DNA interaction as it directly relates to inflammasome assembly using advanced methods in cryo-electron microscopy.[47]

Limitations of the study

The primary limitation of our elaborate study is the absence of animal models to demonstrate how these inhibitors modulate diseases involving the NLRP3 inflammasome in more complex biological systems. Additionally, questions remain regarding the translatability of our findings to clinical settings, especially when simultaneously targeting NLRP3 and hOGG1 to mitigate inflammatory signaling. Moreover, our results are derived from immortalized mouse macrophages in cell culture, which lack the diverse immune cell interactions present *in vivo*. Lastly, employing advanced biophysical techniques, such as cryo-EM to elucidate the interactions of NLRP3 with inhibitors herein could enhance our understanding of their mechanisms and improve drug efficacy.

STAR★METHODS

Detailed methods are provided in the online version of this paper and include the following:

- KEY RESOURCES TABLE
- RESOURCE AVAILABILITY
  - Lead contact
  - Materials availability
  - Data and code availability
- EXPERIMENTAL MODEL AND STUDY PARTICIPANT DETAILS
  - Cell lines
- METHOD DETAILS
  - Purification and expression of NLRP3$_{1-93}$
  - Wild-type NLRP3 and NACHT-LRR expression and purification
  - DNA cleavage assay
  - hOGG1 inhibitor and salmon sperm DNA competition pulldown
  - Protein thermostability assay
  - SWISS-MODEL generation of hOGG1-based NLRP3 active model

○ Fluorescence polarization
○ Isolation of cytosolic, mitochondrial, and whole-cell DNA in wild-type and knockout mouse iBMDMs
○ Amplification of 591 bp and 5489 bp fragments from purified DNA from the mitochondria and cytosol of iBMDMs
○ Mouse macrophage cell culture
○ Macrophage inflammasome activation with inhibitors
○ Measurement of macrophage cell viability after treatment
○ Real-time PCR (qPCR) analysis of mtDNA in the cytosol of iBMDMs
○ Electrostatic potential map of wild type NLRP3 PYD and D21H PYD
● QUANTIFICATION AND STATISTICAL ANALYSIS

SUPPLEMENTAL INFORMATION

Supplemental information can be found online at https://doi.org/10.1016/j.isci.2024.110459.

AUTHOR CONTRIBUTIONS

A.L performed drug binding pulldowns, thermal shift assays, fluorescence polarization, and inflammasome activation studies. J.E.C. performed cleavage assays, fluorescence polarization, and sequence alignments. Y.Q., H.Z., L.L., M.P., A.M., S.L., and E.A. helped J.E.C. and A.L. with Bradfords and western blots. R.M. and A.L. made molecular models. R.M. designed experiments and supervised the project. A.L., J.E.C, and R.M. conceived of the study. R.M. wrote the article. A.L., J.E.C, and R.M. edited the article with input from all authors.

DECLARATION OF INTERESTS

UCI is in the process of submitting a patent covering the use of repurposed anti-inflammatory drugs targeting NLRP3 listing A.L, J.C, and R.M as inventors. All other authors declare no competing interests.

REFERENCES

1. Pandori, W.J., Lima, T.S., Mallya, S., Kao, T.H., Gov, L., and Lodoen, M.B. (2019). Toxoplasma gondii activates a Syk-CARD9-NF-κB signaling axis and gasdermin D-independent release of IL-1β during infection of primary human monocytes. PLoS Pathog. 15, e1007923. https://doi.org/10.1371/journal.ppat.1007923.

2. Dostert, C., Pétrilli, V., Van Bruggen, R., Steele, C., Mossman, B.T., and Tschopp, J. (2008). Innate immune activation through Nalp3 inflammasome sensing of asbestos and silica. Science 320, 674–677. https://doi.org/10.1126/science.1156995.

3. Hoffman, H.M., Mueller, J.L., Broide, D.H., Wanderer, A.A., and Kolodner, R.D. (2001). Mutation of a new gene encoding a putative pyrin-like protein causes familial cold autoinflammatory syndrome and Muckle-Wells syndrome. Nat. Genet. 29, 301–305. https://doi.org/10.1038/ng756.

4. Xiao, L., Magupalli, V.G., and Wu, H. (2023). Cryo-EM structures of the active NLRP3 inflammasome disc. Nature 613, 595–600. https://doi.org/10.1038/s41586-022-05570-8.

5. Gross, O., Thomas, C.J., Guarda, G., and Tschopp, J. (2011). The inflammasome: an integrated view. Immunol. Rev. 243, 136–151. https://doi.org/10.1111/j.1600-065X.2011.01046.x.

6. Liu, X., Zhang, Z., Ruan, J., Pan, Y., Magupalli, V.G., Wu, H., and Lieberman, J. (2016). Inflammasome-activated gasdermin D causes pyroptosis by forming membrane pores. Nature 535, 153–158. https://doi.org/10.1038/nature18629.

7. Netea, M.G., Nold-Petry, C.A., Nold, M.F., Joosten, L.A., Opitz, B., van der Meer, J.H., van de Veerdonk, F.L., Ferwerda, G., Heinhuis, B., Devesa, I., et al. (2009). Differential requirement for the activation of the inflammasome for processing and release of IL-1beta in monocytes and macrophages. Blood 113, 2324–2335. https://doi.org/10.1182/blood-2008-03-146720.

8. Bauernfeind, F.G., Horvath, G., Stutz, A., Alnemri, E.S., MacDonald, K., Speert, D., Fernandes-Alnemri, T., Wu, J., Monks, B.G., Fitzgerald, K.A., et al. (2009). Cutting edge: NF-kappaB activating pattern recognition and cytokine receptors license NLRP3 inflammasome activation by regulating NLRP3 expression. J. Immunol. 183, 787–791. https://doi.org/10.4049/jimmunol.0901363.

9. Zhong, Z., Liang, S., Sanchez-Lopez, E., He, F., Shalapour, S., Lin, X.J., Wong, J., Ding, S., Seki, E., Schnabl, B., et al. (2018). New mitochondrial DNA synthesis enables NLRP3 inflammasome activation. Nature 560, 198–203. https://doi.org/10.1038/s41586-018-0372-z.

10. Pastukh, V.M., Gorodnya, O.M., Gillespie, M.N., and Ruchko, M.V. (2016). Regulation of mitochondrial genome replication by hypoxia: The role of DNA oxidation in D-loop region. Free Radic. Biol. Med. 96, 78–88. https://doi.org/10.1016/j.freeradbiomed.2016.04.011.

11. Zhong, Z., Umemura, A., Sanchez-Lopez, E., Liang, S., Shalapour, S., Wong, J., He, F., Boassa, D., Perkins, G., Ali, S.R., et al. (2016). NF-κB Restricts Inflammasome Activation via Elimination of Damaged Mitochondria. Cell 164, 896–910. https://doi.org/10.1016/j.cell.2015.12.057.

12. Tumurkhuu, G., Shimada, K., Dagvadorj, J., Crother, T.R., Zhang, W., Luthringer, D., Gottlieb, R.A., Chen, S., and Arditi, M. (2016). Ogg1-Dependent DNA Repair Regulates NLRP3 Inflammasome and Prevents Atherosclerosis. Circ. Res. 119, e76–e90. https://doi.org/10.1161/CIRCRESAHA.116.308362.

13. Xian, H., Watari, K., Sanchez-Lopez, E., Offenberger, J., Onyuru, J., Sampath, H., Ying, W., Hoffman, H.M., Shadel, G.S., and Karin, M. (2022). Oxidized DNA fragments exit mitochondria via mPTP- and VDAC-dependent channels to activate NLRP3 inflammasome and interferon signaling. Immunity 55, 1370–1385.e8. https://doi.org/10.1016/j.immuni.2022.06.007.

14. Cabral, A., Cabral, J.E., Wang, A., Zhang, Y., Liang, H., Nikbakht, D., Corona, L., Hoffman, H.M., and McNulty, R. (2023). Differential Binding of NLRP3 to non-oxidized and Ox-mtDNA mediates NLRP3 Inflammasome Activation. Commun. Biol. *6*, 578. https://doi.org/10.1038/s42003-023-04817-y.

15. Bruner, S.D., Norman, D.P., and Verdine, G.L. (2000). Structural basis for recognition and repair of the endogenous mutagen 8-oxoguanine in DNA. Nature *403*, 859–866. https://doi.org/10.1038/35002510.

16. Nash, H.M., Lu, R., Lane, W.S., and Verdine, G.L. (1997). The critical active-site amine of the human 8-oxoguanine DNA glycosylase, hOgg1: direct identification, ablation and chemical reconstitution. Chem. Biol. *4*, 693–702. https://doi.org/10.1016/s1074-5521(97)90225-8.

17. Whitaker, A.M., Flynn, T.S., and Freudenthal, B.D. (2018). Molecular snapshots of APE1 proofreading mismatches and removing DNA damage. Nat. Commun. *9*, 399. https://doi.org/10.1038/s41467-017-02175-y.

18. Chou, K.M., and Cheng, Y.C. (2002). An exonucleolytic activity of human apurinic/apyrimidinic endonuclease on 3' mispaired DNA. Nature *415*, 655–659. https://doi.org/10.1038/415655a.

19. Roychoudhury, S., Pramanik, S., Harris, H.L., Tarpley, M., Sarkar, A., Spagnol, G., Sorgen, P.L., Chowdhury, D., Band, V., Klinkebiel, D., and Bhakat, K.K. (2020). Endogenous oxidized DNA bases and APE1 regulate the formation of G-quadruplex structures in the genome. Proc. Natl. Acad. Sci. USA *117*, 11409–11420. https://doi.org/10.1073/pnas.1912355117.

20. Meng, E.C., Goddard, T.D., Pettersen, E.F., Couch, G.S., Pearson, Z.J., Morris, J.H., and Ferrin, T.E. (2023). UCSF ChimeraX: Tools for structure building and analysis. Protein Sci. *32*, e4792. https://doi.org/10.1002/pro.4792.

21. Dyson, H.J., and Wright, P.E. (2016). Role of Intrinsic Protein Disorder in the Function and Interactions of the Transcriptional Coactivators CREB-binding Protein (CBP) and p300. J. Biol. Chem. *291*, 6714–6722. https://doi.org/10.1074/jbc.R115.692020.

22. Oates, M.E., Romero, P., Ishida, T., Ghalwash, M., Mizianty, M.J., Xue, B., Dosztanyi, Z., Uversky, V.N., Obradovic, Z., Kurgan, L., et al. (2013). D²P²: database of disordered protein predictions. Nucleic Acids Res. *41*, D508–D516. https://doi.org/10.1093/nar/gks1226.

23. Nash, H.M., Bruner, S.D., Scharer, O.D., Kawate, T., Addona, T.A., Spooner, E., Lane, W.S., and Verdine, G.L. (1996). Cloning of a yeast 8-oxoguanine DNA glycosylase reveals the existence of a base-excision DNA-repair protein superfamily. Curr. Biol. *6*, 968–980. https://doi.org/10.1016/s0960-9822(02)00641-3.

24. Norman, D.P., Chung, S.J., and Verdine, G.L. (2003). Structural and biochemical exploration of a critical amino acid in human 8-oxoguanine glycosylase. Biochemistry *42*, 1564–1572. https://doi.org/10.1021/bi026823d.

25. Sidorenko, V.S., Grollman, A.P., Jaruga, P., Dizdaroglu, M., and Zharkov, D.O. (2009). Substrate specificity and excision kinetics of natural polymorphic variants and phosphomimetic mutants of human 8-oxoguanine-DNA glycosylase. FEBS J. *276*, 5149–5162. https://doi.org/10.1111/j.1742-4658.2009.07212.x.

26. Mao, G., Pan, X., Zhu, B.B., Zhang, Y., Yuan, F., Huang, J., Lovell, M.A., Lee, M.P., Markesbery, W.R., Li, M., and Gu, L. (2007). Identification and characterization of OGG1 mutations in patients with Alzheimer's disease. Nucleic Acids Res. *35*, 2759–2766. https://doi.org/10.1093/nar/gkm189.

27. Waterhouse, A., Bertoni, M., Bienert, S., Studer, G., Tauriello, G., Gumienny, R., Heer, F.T., de Beer, T.A.P., Rempfer, C., Bordoli, L., et al. (2018). SWISS-MODEL: homology modelling of protein structures and complexes. Nucleic Acids Res. *46*, W296–W303. https://doi.org/10.1093/nar/gky427.

28. Shimada, K., Crother, T.R., Karlin, J., Dagvadorj, J., Chiba, N., Chen, S., Ramanujan, V.K., Wolf, A.J., Vergnes, L., Ojcius, D.M., et al. (2012). Oxidized mitochondrial DNA activates the NLRP3 inflammasome during apoptosis. Immunity *36*, 401–414. https://doi.org/10.1016/j.immuni.2012.01.009.

29. Visnes, T., Cazares-Korner, A., Hao, W., Wallner, O., Masuyer, G., Loseva, O., Mortusewicz, O., Wiita, E., Sarno, A., Manoilov, A., et al. (2018). Small-molecule inhibitor of OGG1 suppresses proinflammatory gene expression and inflammation. Science *362*, 834–839. https://doi.org/10.1126/science.aar8048.

30. Tahara, Y.K., Auld, D., Ji, D., Beharry, A.A., Kietrys, A.M., Wilson, D.L., Jimenez, M., King, D., Nguyen, Z., and Kool, E.T. (2018). Potent and Selective Inhibitors of 8-Oxoguanine DNA Glycosylase. J. Am. Chem. Soc. *140*, 2105–2114. https://doi.org/10.1021/jacs.7b09316.

31. Booshehri, L.M., and Hoffman, H.M. (2019). CAPS and NLRP3. J. Clin. Immunol. *39*, 277–286. https://doi.org/10.1007/s10875-019-00638-z.

32. Xian, H., and Karin, M. (2023). Oxidized mitochondrial DNA: a protective signal gone awry. Trends Immunol. *44*, 188–200. https://doi.org/10.1016/j.it.2023.01.006.

33. Eslam, M., Newsome, P.N., Sarin, S.K., Anstee, Q.M., Targher, G., Romero-Gomez, M., Zelber-Sagi, S., Wai-Sun Wong, V., Dufour, J.F., Schattenberg, J.M., et al. (2020). A new definition for metabolic dysfunction-associated fatty liver disease: An international expert consensus statement. J. Hepatol. *73*, 202–209. https://doi.org/10.1016/j.jhep.2020.03.039.

34. Todoric, J., Di Caro, G., Reibe, S., Henstridge, D.C., Green, C.R., Vrbanac, A., Ceteci, F., Conche, C., McNulty, R., Shalapour, S., et al. (2020). Fructose stimulated de novo lipogenesis is promoted by inflammation. Nat. Metab. *2*, 1034–1045. https://doi.org/10.1038/s42255-020-0261-2.

35. Bottini, N., and Firestein, G.S. (2013). Duality of fibroblast-like synoviocytes in RA: passive responders and imprinted aggressors. Nat. Rev. Rheumatol. *9*, 24–33. https://doi.org/10.1038/nrrheum.2012.190.

36. Minns, M.S., Liboro, K., Lima, T.S., Abbondante, S., Miller, B.A., Marshall, M.E., Tran Chau, J., Roistacher, A., Rietsch, A., Dubyak, G.R., and Pearlman, E. (2023). NLRP3 selectively drives IL-1β secretion by Pseudomonas aeruginosa infected neutrophils and regulates corneal disease severity. Nat. Commun. *14*, 5832. https://doi.org/10.1038/s41467-023-41391-7.

37. Jumper, J., Evans, R., Pritzel, A., Green, T., Figurnov, M., Ronneberger, O., Tunyasuvunakool, K., Bates, R., Žídek, A., Potapenko, A., et al. (2021). Highly accurate protein structure prediction with AlphaFold. Nature *596*, 583–589. https://doi.org/10.1038/s41586-021-03819-2.

38. Collins, L.V., Hajizadeh, S., Holme, E., Jonsson, I.M., and Tarkowski, A. (2004). Endogenously oxidized mitochondrial DNA induces in vivo and in vitro inflammatory responses. J. Leukoc. Biol. *75*, 995–1000. https://doi.org/10.1189/jlb.0703328.

39. Kukat, C., Davies, K.M., Wurm, C.A., Spahr, H., Bonekamp, N.A., Kuhl, I., Joos, F., Polosa, P.L., Park, C.B., Posse, V., et al. (2015). Cross-strand binding of TFAM to a single mtDNA molecule forms the mitochondrial nucleoid. Proc. Natl. Acad. Sci. USA *112*, 11288–11293. https://doi.org/10.1073/pnas.1512131112.

40. West, A.P., and Shadel, G.S. (2017). Mitochondrial DNA in innate immune responses and inflammatory pathology. Nat. Rev. Immunol. *17*, 363–375. https://doi.org/10.1038/nri.2017.21.

41. Roers, A., Hiller, B., and Hornung, V. (2016). Recognition of Endogenous Nucleic Acids by the Innate Immune System. Immunity *44*, 739–754. https://doi.org/10.1016/j.immuni.2016.04.002.

42. West, A.P., Khoury-Hanold, W., Staron, M., Tal, M.C., Pineda, C.M., Lang, S.M., Bestwick, M., Duguay, B.A., Raimundo, N., MacDuff, D.A., et al. (2015). Mitochondrial DNA stress primes the antiviral innate immune response. Nature *520*, 553–557. https://doi.org/10.1038/nature14156.

43. Blasius, A.L., and Beutler, B. (2010). Intracellular toll-like receptors. Immunity *32*, 305–315. https://doi.org/10.1016/j.immuni.2010.03.012.

44. Pazmandi, K., Agod, Z., Kumar, B.V., Szabo, A., Fekete, T., Sogor, V., Veres, A., Boldogh, I., Rajnavolgyi, E., Lanyi, A., and Bacsi, A. (2014). Oxidative modification enhances the immunostimulatory effects of extracellular mitochondrial DNA on plasmacytoid dendritic cells. Free Radic. Biol. Med. *77*, 281–290. https://doi.org/10.1016/j.freeradbiomed.2014.09.028.

45. Hochheiser, I.V., Pilsl, M., Hagelueken, G., Moecking, J., Marleaux, M., Brinkschulte, R., Latz, E., Engel, C., and Geyer, M. (2022). Structure of the NLRP3 decamer bound to the cytokine release inhibitor CRID3. Nature *604*, 184–189. https://doi.org/10.1038/s41586-022-04467-w.

46. Chen, J., and Chen, Z.J. (2018). PtdIns4P on dispersed trans-Golgi network mediates NLRP3 inflammasome activation. Nature *564*, 71–76. https://doi.org/10.1038/s41586-018-0761-3.

47. Cabral, A., Cabral, J.E., and McNulty, R. (2022). Cryo-EM for Small Molecules. Curr. Protoc. *2*, e632. https://doi.org/10.1002/cpz1.632.

48. Hornung, V., Bauernfeind, F., Halle, A., Samstad, E.O., Kono, H., Rock, K.L., Fitzgerald, K.A., and Latz, E. (2008). Silica crystals and aluminum salts activate the NALP3 inflammasome through phagosomal destabilization. Nat. Immunol. *9*, 847–856. https://doi.org/10.1038/ni.1631.

STAR★METHODS

KEY RESOURCES TABLE

REAGENT or RESOURCE	SOURCE	IDENTIFIER
Antibodies		
NLRP3 (pyrin targeting)	Adipogen	AG-20B-0014-C100; RRID: AB_2490202
NLRP3 (NACHT targeting)	Cell Signaling	15101; RRID: AB_2722591
Cleaved-IL-1β (Asp117)	Cell Signaling	63124; RRID: AB_2799639
Caspase-1 (p20)	AdipoGen	AG-20B-0042-C100; RRID: AB_2490248
OGG1	Santa Cruz Biotechnology	sc-376935
FEN1	Santa Cruz Biotechnology	sc-28355; RRID: AB_627587
beta-Actin	Santa Cruz Biotechnology	sc-47778; RRID: AB_626632
Anti-rabbit IgG, HRP-linked	Cell Signaling	7074; RRID: AB_2099233
Anti-mouse IgG, HRP-linked	Cell Signaling	7076; RRID: AB_330924
Streptavidin HRP-linked antibody	BD Parmingen	554066; RRID: AB_286972
Bacterial and virus strains		
DH5a cells/kit	NEB	E0554S
Chemicals, peptides, and recombinant proteins		
Bovine Serum Albumin	Gemini	Cat#700-100
APE1	NEB	M0282S
TH5487	Selleck Chemicals	S8913
SU0268	MedChemExpress	HY-139056
Recombinant Human OGG1 protein	Abcam	ab98249
Critical commercial assays		
8-hydroxy 2 deoxyguanosine ELISA Kit	Abcam	ab201734
Protein Thermal Shift™ Dye Kit	ThermoFisher	4461146
SsoAdvanced Universal SYBR® Green Supermix	BioRad	1725270
Site-directed mutagenesis Kit	Agilent	210518
Phusion Hot Start Flex 2X Master Mix	NEB	M0536
ExpiFectamine™ 293 Transfection Kit	ThermoFisher	A14525
PureLink™ HiPure Plasmid Maxiprep Kit	ThermoFisher	K210007
Zymo Quick-DNA Miniprep kit	Zymo	D3025
Experimental models: Cell lines		
Expi293F™ Cells	ThermoFisher (Gibco)	A14527
Immortalized Mouse Macrophages	Dr. Michael Karin (UCSD)	N/A
Immortalized Mouse Macrophages - NLRP3 Knockout	Dr. Michael Karin (UCSD)	N/A
Oligonucleotides		
90 base-pair oxidized mitochondrial DNA (biotinylated): (Biotin-AAT CTA CCA TCC TCC/i8oxodG/T/i8oxodG/AAA CCA ACA ACC C/i8oxodG/C CCA CCA AT/i8oxodG/CCC CTC TTC TC/i8oxodG/CTC C/i8oxodG// i8oxodG//i8oxodG/CC CAT TAA ACT T/i8oxodG//i8oxodG// i8oxodG//i8oxodG//i8oxodG/TA/i8oxodG/CTA AAC T/i8oxodG/A)	IDT	N/A
20 base-pair oxidized mitochondrial DNA (biotinylated): (Biotin- AAT CTA CCA TCC TCC/i8oxodG/T/i8oxodG/AA)	IDT	N/A
20 base-pair oxidized mitochondrial DNA: (AAT CTA CCA TCC TCC/i8oxodG/T/i8oxodG/AA)	IDT	N/A

Continued

REAGENT or RESOURCE	SOURCE	IDENTIFIER
20 base-pair non-oxidized mitochondrial DNA (biotinylated): (Biotin-AAT CTA CCA TCC TCC GTG AA)	IDT	N/A
20 base-pair non-oxidized mitochondrial DNA: (AAT CTA CCA TCC TCC GTG AA)	IDT	N/A
20 base-pair oxidized Cy5: (AAT CTA CCA/i8oxodG/TC CTC CCT CA/3Cy5Sp/)	IDT	N/A
Sonicated Salmon Sperm	Stratagene	201190-81
Recombinant DNA		
NLRP3	Dr. Hal Hoffman (UCSD)	N/A
NLRP3 D21H Full length	In-house mutagenesis	N/A
NLRP3 PYD$_{(1-93)}$	In-house mutagenesis	N/A
NLRP3 NACHT-LRR$_{(94-1043)}$	In-house mutagenesis	N/A
Software and algorithms		
PRISM 10	GraphPad Software	N/A
ImageJ	Image J	N/A
BioRad Duet Maestro Software	BioRad	N/A
BioTek Gen6	Agilent	N/A
iBright Analysis Software	ThermoFisher	N/A
ChimeraX	UCSF	N/A
SWISS-MODEL	Expasy	N/A
Other		
DMEM	ThermoFisher	11966025
Fetal Bovine Serum (FBS), heat innactivated	ThermoFisher	A5256801
Penicillin-streptomycin	ThermoFisher	10378016
LPS	ThermoFisher	m00-4976-03

RESOURCE AVAILABILITY

Lead contact

Further information and requests for resources and reagents should be directed to and will be fulfilled by the lead contact, Dr. Reginald McNulty (rmcnulty@uci.edu).

Materials availability

Materials generated in this study are available upon reasonable request from the lead contact Dr. Reginald McNulty (rmcnulty@uci.edu).

Data and code availability

- All key reagents and resources are listed in the key resources table.
- Any additional information required to reanalyze the data reported in this paper is available from the lead contact upon request.
- This paper does not report original code.

EXPERIMENTAL MODEL AND STUDY PARTICIPANT DETAILS

Cell lines

Expi293 cells were purchased from ThermoFisher (#A14527). Wild-type and NLRP3 knockout iBMDM mouse cells were generated by Katherine Fitzgerald (UMass) from wild-type (C57BL/6), or NLRP3-deficient mice.[48] All cell lines used in this study were negative for mycoplasma.

METHOD DETAILS

Purification and expression of NLRP3$_{1-93}$

Site-directed mutagenesis (Agilent #210518) was performed on wild type NLRP3 to introduce a stop codon following the 93rd amino acid, isolating the pyrin domain as previously explained.[14] Briefly, NLRP3$_{1-93}$ was cloned in the mammalian expression vector pcDNA3.1HisB. The plasmid was then sequenced, grown at large scale, and purified with PureLink HiPure Expi Megaprep. The protein was expressed in 250 mL of media using the Expi293$_{TM}$ Expression System (Thermo Fisher). Enhancers were added 16 h after transfection. Once the cells reached viability of <80% live cells, they were harvested by spinning at 1200 rpm in a swinging bucket rotor (JS-4.750, Beckman). After centrifugation, the dead cells were aspirated, and the pellet was resuspended in cold PBS to remove residual media. The protein was purified with half of the cell pellet on the AKTA Advant. Cells were resuspended in lysis buffer containing (50 mM Tris-HCl pH 7.4, 1X protease inhibitor (Pierce), 0.1% SDS, 10% glycerol, and 1% Triton X-100). The lysate was then sonicated for 42 s in intervals of 2 s on and 8 s off. Lysate was then clarified by spinning at 100,000 x g for 1 h and subsequently passed through a 0.45 μm filter prior to affinity chromatography. The HisTrap FF crude 5 mL column was equilibrated in Buffer A (20 mM Tris pH 7.4, 200 mM NaCl, 10% glycerol) and eluted with Buffer B (20 mM Tris pH 7.4, 200 mM NaCl, 10% glycerol, 500 mM imidazole, 1 mM DTT, and 0.5% NP-40). The column was washed with Buffer A and eluted in a 5-step gradient of Buffer B (5%, 15%, 25%, 50%, 100%). Peak fractions were analyzed on a total protein NuPAGE 4–12% Bis-Tris run at 200 V for 30 min. Fractions were further analyzed with PVDF membrane western blots blocked in 2.5% BSA and probed with monoclonal pyrin targeting antibody (Adipogen) at a dilution of 1:10,000. Based on the result from the above gels, fractions were pooled and loaded onto a HiLoad 16/600 Superose 6 size exclusion column (20 mM Tris pH 7.4, 200 mM NaCl, 10% glycerol, 1 mM DTT, and 0.5% NP-40). No distinguishable peaks exist due to the presence of NP-40 in the buffer, thus all fractions were run on SDS page and western blots, and the NLRP3$_{1-93}$ sample was further analyzed via Native 4–16% gel (Figure S11). Protein concentrations were checked via Bradford (Biorad) to a final concentration of roughly 1 mg/mL.

Wild-type NLRP3 and NACHT-LRR expression and purification

Wild-type NLRP3 was cloned into the mammalian expression vector pcDNA3.1HisB. The plasmid was expressed in DH5α cells (New England Biolabs) and purified using the PureLink HiPure Plasmid Maxiprep Kit (Thermo Fisher). The protein was expressed using the Expi293 Expression System (Thermo Fisher) per the manufacturer's instructions. Briefly, cells were grown in Expi293 expression media until they reached a concentration of 3×10^6 cells per milliliter and sustained viability of ≥95% live cells. At that time, 1 μg of expression vector was transfected per every 1 mL of cells with Expifectamine reagent. Once the cells reached viability of ≤80% live cells, they were harvested by spinning at 300 rpm for 5 min. The supernatant/dead cells were aspirated from the top, and the pellet was washed with cold PBS. The cells were pelleted again at 1200 rpm for 5 min and lysed with 50 mM Tris pH 7.4, 1 mM PMSF, 1 x protease and phosphatase inhibitor, 300 mM NaCl, 0.1% SDS, 10% glycerol, and 1% Triton X-100. The lysate was sonicated for 42 s in intervals of 2 s on, 8 s off, then clarified by spinning at 100,000 × g for 60 min. The clarified lysate was passed through a 0.45 μm filter and purified using a HisTrap FF crude 5 mL column. The column was pre-equilibrated with 20 mM Tris, 200 mM NaCl, 10% glycerol, 1 mM DTT, and 25 mM imidazole, pH 7.4. After the sample was loaded onto the column, it was washed with 10 column volumes (CV) of the wash buffer above. Then, using a four-step gradient from 25 to 100%, the protein was eluted using 20 mM Tris, 200 mM NaCl, 10% glycerol, 1 mM DTT, and 500 mM Imidazole, at pH 7.4. Peak fractions were pooled and loaded onto a HiLoad 16/600 Superose 6 pg size exclusion column. The column was run in a buffer containing 20 mM Tris, 200 mM NaCl, 10% glycerol, and 1 mM DTT, pH 7.4. Peak fractions were analyzed by SDS page and western blot. Samples were diluted with LDS sample loading buffer and reducing agent (Invitrogen), each at a final concentration of 1x. The samples were boiled at 90°C and run on a NuPAGE 4 to 12%, Bis-Tris 1 mM 15-well mini-gels at 200 V for 30 min. For the western blot, samples were transferred to PVDF membranes, and blocked with 2.5% BSA. NLRP3 was probed with an anti-NLRP3 antibody (AdipoGen) at a 1:10,000 dilution in 2.5% BSA in TBST. NACHT-LRR$_{(94-1043)}$ was probed with a different anti-NLRP3 antibody (Cell Signaling) at a 1:1000 dilution in 2.5% BSA. Blots were incubated with an HRP-linked anti-mouse (Cell Signaling) or rabbit (Cell Signaling) secondary antibodies at 1:1,000 dilutions and imaged using the iBright 1500 Imaging system. Once peak fractions were identified, they were pooled and concentrated using 100 kDa cut-off spin concentrators at cycles of 2000 × g for 5 min.

DNA cleavage assay

The DNA cleavage assay was performed with the purified pyrin domain and NACHT-LRR$_{94-1043}$ constructs. NLRP3 pyrin$_{(1-93)}$ was dialyzed into buffer (150 mM NaCl, 20 mM Tris, 0.05% NP-40, 1 mM DTT, pH 7.4) with a 10 kDa MWCO (Thermo). The NACHT-LRR$_{94-1043}$ construct remained in the size exclusion buffer for the DNA cleavage assay. Biotinylated ox-mtDNA, sourced from IDT, was diluted in DEPC water to 2.7 ng/μL. Pyrin protein was added to ox-mtDNA either with or without APE1 at a final concentration of 0.0784 mg/mL. The NACHT-LRR construct was incubated at concentrations ranging from 0.0125 mg/mL to 0.4 mg/mL. In samples containing APE1 (NEB #M0282S), DNA and protein was first incubated on ice for 30 min. After incubation, 5 units of APE1 and 10% NEB4 magnesium buffer were combined with the ox-mtDNA/protein solution. All samples were warmed at 37°C for 16 h and further incubated at 4°C for approximately 80 h prior to being analyzed on a 4–20% Tris-Glycine gel (Thermo), with a total reaction volume of 25 μL. Initial attempts to determine if ox-mtDNA cleavage by the pyrin domain was temperature dependent, prompted full incubation at 4°C. Samples were boiled in 10% formamide and 1X Orange Loading Dye containing SDS (NEB) for 2 min at 90°C. The gel was loaded with Orange Loading Dye (NEB) and pre-run for 30 min at 100 V. The gel was run with 5 μL of reaction for 35 min at 225 V and transferred to an Immobilon-P 0.45 μm PVDF membrane (Millipore). After being transferred, the DNA was UV crosslinked for 10 min and blocked in 2.5% BSA and TBST (150 mM NaCl, 20 mM Tris, 0.1% Tween pH

7.4). The membrane was then probed with streptavidin HRP-linked antibody 1:2000 (BD Parmingen #554066) and washed 3 times in TBST for 10 min. Chemiluminescence (Thermo) was performed, and the DNA imaged with IBright and further analyzed in IBright software.

hOGG1 inhibitor and salmon sperm DNA competition pulldown

Dynabeads M-280 Streptavidin (Thermo Fisher) were removed from the storage solution and washed three times with binding buffer (50 mM Tris, 100 mM NaCl, 2 mM MgCl$_2$, 12% glycerol, and pH 7.4) using a DynaMag-2 magnet. Biotinylated Ox-mtDNA sourced from IDT was diluted 4:400 from the 100 μM stock solution and incubated with the beads overnight at 4°C while rotating. The following day, inhibitors TH5487 (Selleck Chemicals) and SU0268 (MedChemExpress) were serial diluted with binding buffer such that the addition of inhibitor at various concentrations was always 10% of the final volume. Then the inhibitor was incubated with the protein (NLRP3, NACHT-LRR$_{(94-1034)}$, or pyrin$_{(1-93)}$) at various concentrations from 1 nM to 100 μM at 4°C for 1 h. A control of protein with binding buffer was also incubated at 4°C for 1 h. After? these incubations, the beads were separated on the magnet and washed three times with binding buffer to remove any unbound DNA. Once the inhibitor incubations were complete, each incubation was added to a well with beads in triplicate, mixed by pipetting up and down, and incubated at 4°C overnight. The following day, the beads were separated on the magnet, the supernatant was removed, and the beads were washed three times with binding buffer. To evaluate the amount of NLRP3 bound to the beads, the beads were resuspended in LDS sample loading buffer and reducing agent (Invitrogen), each at a final concentration of 1X. The samples were boiled at 90°C and run on NuPAGE 4 to 12%, Bis-Tris 1 mM 15-well mini-gels at 200 V for 30 min. Samples were transferred to PVDF membranes and blocked with 2.5% BSA. Pyrin$_{(1-93)}$ and NLRP3 westerns were probed with an anti-NLRP3 antibody (AdipoGen) at a 1:10,000 dilution in 2.5% BSA in TBST. NACHT-LRR$_{(94-1034)}$ westerns were probed with a different anti-NLRP3 antibody (Cell Signaling) at a 1:1000 dilution in 2.5% BSA. Blots were incubated with an HRP-linked anti-mouse (Cell Signaling) or anti-rabbit (Cell Signaling) secondary antibodies for 1 h at a 1:1,000 dilutions and imaged using the iBright 1500 Imaging system. The intensities of the bands were quantified using the iBright Analysis Software. The intensity values were plotted and analyzed using GraphPad Prism and a one-way ANOVA.

Protein thermostability assay

NLRP3, NACHT-LRR$_{(94-1034)}$, pyrin$_{(1-93)}$, and aldolase proteins were diluted to 1 mg/mL and challenged with 100 or 1000 μM TH5487 (Selleck Chemicals) or SU0268 (MedChemExpress) diluted in 20 mM Tris, 200 mM NaCl, 10% glycerol, and 1 mM DTT, pH 7.4 for 1 h at 4°C. Each protein was also incubated with buffer alone as a control. During this incubation, the assay plate was set up. Plates (BioRad, #HSP9601) were set up in the dark on ice using the Protein Thermal Shift Dye Kit (Thermo Fisher, #4461146) per the manufacturer's instructions. Briefly, protein thermal shift dye was diluted to 8X, and 2.5 μL was added to each sample well along with 5 μL of protein thermal shift buffer. Once the protein incubations were completed, 12.5 μL was added to the sample wells in quadruplicate. Wells were mixed by pipetting up and down 3 times with a multichannel pipette, then spun down at 1000 rpm for 2 min. The plate was kept in the dark and on ice until analysis. Melting temperature analysis was done using a CFX Duet Real-Time PCR system (BioRad, #12016265) and the CFX Maestro Software 2.3 (BioRad, #12013758). To set-up a thermal shift assay, all other steps of the standard RT-PCR run were removed, and a melt curve was inserted. An initial 30 s at 4°C cycle was inserted before the ramp step. The protocol was set to ramp at a ramp rate of 0.5°C every 10 s from 4°C to 95°C. The FRET channel was assigned to each sample well, and the plate was inserted into the machine and run. The resulting melting temperatures were plotted and analyzed using GraphPad Prism and a one-way ANOVA.

SWISS-MODEL generation of hOGG1-based NLRP3 active model

Using ChimeraX, the published structure of hOGG1 bound to Ox-DNA was opened (PDBID: 1EBM). The amino acid sequence of hOGG1$_{(249-325)}$ that aligned with the NLRP3 pyrin$_{(1-91)}$ domain was saved as a.pdb file. The sequence was uploaded to SWISS-MODEL in their User Template Modeling input option as the template file.[27] Then, NLRP3 amino acids 1–85 were loaded as the target file (amino acids 1–90 did not generate a model). The SWISS-MODEL projection produced one model of NLRP3 based on the template hOGG1 structure. This model was further analyzed in comparison to wild-type NLRP3 and various hOGG1 structures using ChimeraX.[20]

Fluorescence polarization

Stock 100 μM Cy5-labeled 20 base-pair DNA (IDT) was diluted 1:100 to a working stock of 1 μM. Protein was serial diluted from 1 mg/mL stock seven times for 8 total reaction tubes ranging from 0.0075 to 1 mg/mL 10 μL of 1 μM DNA stock was added to 90 μL of each serial diluted protein reaction. 10 μL DNA was also added to 90 μL buffer as a control. These mixtures were incubated on ice for 1 h. After 1 h, each reaction tube was split into three, and 30 μL of each was added in triplicate to three wells of a black-walled, clear-bottomed 384-well plate (Agilent #204623). The wells of buffer were also added as controls. Fluorescence polarization was then read using a BioTek Synergy H1 plate reader with Generation 6 software (Agilent) at an excitation of 620/40 and emission of 680/30, specific to Cy5. The polarization values were calculated based on the parallel and perpendicular light and G-factor-corrected. The raw values were normalized to the DNA alone wells and analyzed using a one-way ANOVA in GraphPad Prism. In experiments containing hOGG1 inhibitors, proteins were pre-incubated with the drugs at a final concentration of 5–50 μM for 1 h on ice before incubation with DNA.

Isolation of cytosolic, mitochondrial, and whole-cell DNA in wild-type and knockout mouse iBMDMs

Knockout or wild-type mouse iBMDMs were treated in the presence or absence of hOGG1 inhibitors as described below. The cytosolic and mitochondrial fractions were isolated as described previously.[13] Briefly, cells were washed with pre-chilled PBS and harvested at 1000 xg for 5 min. 10% of the cells were removed and saved for purification of the whole cell DNA fraction. The washed cells were resuspended in pre-chilled mitochondrial extraction buffer (22 mM mannitol, 70 mM sucrose, 20 mM Tris Base pH 7.5, 1 mM EDTA, 2 mg/mL BSA, and 1 tablet of protease and phosphatase inhibitor (Roche)). Resuspended cells were passed through a 25-G syringe (Fisher #14-817-133) 20 times on ice. The mixture was then spun twice. An initial spin was carried out at 1000 xg for 15 min at 4°C, the pellet was discarded, and the supernatant was centrifuged again at 10,000 xg for 10 min at 4°C. The supernatant was saved for further purification as the cytosolic fraction, and the pellet was saved for further purification of the mitochondrial fraction. Both fractions were purified using the Zymo Quick-DNA Miniprep kit (Zymo #D3025). The mitochondrial fraction and whole cell fractions were purified per the manufacturer's instructions. For the cytosolic fraction, the initial lysis step in the manufacturer's protocol was skipped and started instead at the column loading step. After purification was completed, the DNA concentration was evaluated by reading the A260 in a nanodrop. To visualize total mitochondrial or cytosolic DNA, 200 ng of DNA of each sample was run directly on a 2% agarose gel stained with ethidium bromide. To measure the amount of 8-oxo-dG containing DNA, an ELISA was run on the samples using an 8-oxo-dG ELISA kit (Abcam #ab201734) following the manufacturer's instructions.

Amplification of 591 bp and 5489 bp fragments from purified DNA from the mitochondria and cytosol of iBMDMs

Knockout or wild-type mouse iBMDMs were treated in the presence or absence of hOGG1 inhibitors as described below. Isolation and purification of mitochondrial and cytosolic DNA were completed as described above. PCRs were performed to amplify a larger 5489 bp fragment and the D loop 591 bp fragment from both mitochondrial and cytosolic purified DNA and described previously.[13] Briefly, PCR reactions were set up using the Phusion Hot Start 2x Master Mix (NEB #M0536) per the manufacturer's protocol. For 5698 bp PCRs on the cytosolic fractions, 200 ng of DNA was used as a template. For all other reactions, 5 ng was used as a template. For the PCR reactions, the following settings were used: initial denaturation at 98°C for 3 min, denaturation at 98°C for 10 s, annealing temperature of 60°C, and extension temperature of 72°C for 30 s (591 bp) or 3 min (5698 bp). This ran 20 (591 bp) or 35 (5698 bp) cycles, followed by a final extension of 72°C for 20 min. Amplified products were analyzed on a 2% agarose gels stained with ethidium bromide.

Mouse macrophage cell culture

Immortalized wild-type mouse macrophages were generously provided to us by Michael Karin at the University of California, San Diego. A frozen vial of cells at $1*10^7$ was thawed in a water bath and then resuspended in 50 mL of culture media (DMEM (Thermo Fisher) supplement with 10% heat-inactivated FBS (Sigma) and 1% Penicillin-Streptomycin (Thermo Fisher)). The cells were spun down at 300 xg for 5 min at 4°C, the media was aspirated off the pellet, and the pellet was resuspended in 5 mL of culture media. The cells were counted by diluting 10 μL of cells with 10 μL of Trypan Blue Stain (Thermo Fisher), loading that dilution onto a Countess Cell Counting Chamber Slide (Thermo Fisher), and evaluated using a Countess 3 FL Automated Cell Counter (Thermo Fisher). Cells were then further diluted in culture media such that the final concentration was $0.2*10^6$/mL and plated onto 175 cm^2 culture flasks (Corning) where they were grown at 37°C and 5% humidity. Cells typically doubled in 24–48 h, where they were then scraped from the bottom of the plate using Bio-One Cell Scrapers (Fisher Scientific) and then spun down, counted, and expanded as previously described.

Macrophage inflammasome activation with inhibitors

The viability and concentration of a culture of immortalized mouse macrophages were checked as described above. Cells at viability >95% were diluted to a concentration of $0.5*10^6$ cells/mL, such that they would be at a concentration of $1*10^6$ cells/mL by the next day. Cells were split into 6-well TC-treated plates (Corning) with 2 mL of cells per well and allowed to adhere and grow overnight at 37°C and 5% humidity. The next day, 2 μL/mL of 500X lipopolysaccharide (Thermo Fisher) was added to each well for 1 h at a final concentration of 500 ng/mL. Next, LPS-only wells were harvested, and inhibitors TH5487 (Selleck Chemicals) and SU0268 (MedChemExpress) were serial diluted such that the addition of any concentration of inhibitor was 1% of the final volume of cells. Then the inhibitors were added at concentrations ranging from 0.1 to 100 μM for 1 h. Next, 4 mM ATP was added to each well for 1 h. Cells and supernatant fractions could then be isolated for viability and western blot analysis. To collect samples for western blot analysis, the supernatant was removed from each well and clarified by spinning at 3000 xg for 5 min using 0.22 μm spin filters (Corning). The cells left on the plate were washed with ice-cold PBS and then lysed with RIPA buffer (Boston BioProducts) supplemented with an EDTA-free protease/phosphatase inhibitor cocktail (Roche). The lysis took place for 5 min rocking at 4°C. The lysed cells were then collected into 1.5 mL tubes and spun at 14,000 xg for 15 min. 200 μL of the clarified lysate was removed and saved for western blot analysis. To evaluate proteins secreted from the cells (Caspase-1 p20 and IL-1β), the supernatant fractions were run on western blots. To evaluate proteins expressed inside the cell (NLRP3, pro-Caspase-1, FEN1, hOGG1, and β-actin), the lysate fraction was run. Samples were diluted with LDS sample loading buffer and reducing agent (Invitrogen), each at a final concentration of 1X. The samples were boiled at 90°C and run on NuPAGE 4 to 12%, Bis-Tris 1 mM 15-well mini-gels at 200 V for 30 min. Samples were transferred to PVDF membranes, blocked with 2.5% BSA in TBST, and probed with a primary antibody against the specific protein diluted to the manufacturer's recommendation in 2.5% BSA in TBST (Table S4). Blots were incubated with an HRP-linked secondary antibody (either mouse or rabbit, depending on the species of the primary) and imaged using the iBright 1500 Imaging system. The intensities of the bands were quantified using the iBright Analysis Software. The intensity values were plotted and analyzed using GraphPad Prism and a one-way ANOVA. To measure the amount

of 8-oxo-dG containing DNA in the supernatant, an ELISA was run on the samples using an 8-oxo-dG ELISA kit (Abcam #ab201734) following the manufacturer's instructions with the standards diluted in cell-treatment media.

Measurement of macrophage cell viability after treatment

After completion of the ATP incubation of the macrophage inflammasome activation assay described above, sample wells for viability readings were analyzed. The supernatant from these wells was aspirated and saved for western blots as described above. 1 mL of fresh culture media (DMEM (Thermo Fisher) supplemented with 10% heat-inactivated FBS (Sigma) and 1% Penicillin-Streptomycin (Thermo Fisher)) was pre-warmed to 37°C and was added to each well. The cells were scraped off the plates using new Bio-One Cell Scrapers (Fisher Scientific) for each well. The now resuspended cells were then moved into 1.5 mL tubes The cells were counted by diluting 10 μL of cells with 10 μL of Trypan Blue Stain (Thermo Fisher), loading that dilution onto a Countess Cell Counting Chamber Slide (Thermo Fisher), and evaluated using a Countess 3 FL Automated Cell Counter (Thermo Fisher). The percent viabilities were recorded in triplicate, and the values were plotted and analyzed using GraphPad Prism and a one-way ANOVA. The remaining cells were spun down at 300 xg for 5 min at 4°C. The supernatant was aspirated, and the cells were washed with ice-cold PBS. To remove the PBS, the cells were spun again at 300 xg for 5 min at 4°C and the PBS was aspirated. The cells were lysed with RIPA buffer (Boston BioProducts) supplemented with an EDTA-free protease/phosphatase inhibitor cocktail (Roche) for 5 min rotating at 4°C. The lysate was clarified by spinning at 14,000 xg for 15 min. 200 μL of the clarified lysate was removed and saved for western blot analysis as described above.

Real-time PCR (qPCR) analysis of mtDNA in the cytosol of iBMDMs

qPCR reactions were set-up with primers for *D loop* DNA, *mCox1* DNA, or *mTert* DNA and DNA extracted from the whole cell, mitochondria, or cytosol using the SsoAdvanced Universal SYBR Green Supermix (BioRad # 1725270) per the manufacturer's instructions. The qPCR reactions were run on the CFX Duet Real-Time PCR machine using the following conditions: Initial denaturation at 98°C for 3 min, then 40 cycles of denaturation at 98°C for 15 s and annealing at 60°C for 30 s. This was followed by a melt curve from 65°C to 95°C with 0.5°C steps and 5 s per step. The readout was visualized using the BioRad CFX Maestro Software. The Cq values obtained for mtDNA abundance in whole cell extracts served as normalization controls for the mtDNA values obtained from the cytosolic fractions. The final ΔΔCq were plotted and analyzed using GraphPad prism and a one-way ANOVA.

Electrostatic potential map of wild type NLRP3 PYD and D21H PYD

To determine the charge for amino acid side chains at pH 7, the pdb of NLRP3 was opened in ChimeraX (PDBID: 7PZC). A pdb file was generated of only the NLRP3 pyrin domain 1-93. To generate the D21H pdb mutation in ChimeraX, the rotamer without any steric clashes and highest prevalence was selected. Both pdb's were then individually uploaded to the APBS-PDB2PQR software suite to generate both.pqr and -pot.dx files. These files were then opened in ChimeraX to generate the electrostatic potential map. The pdb file for the published structure of hOGG1 bound to double stranded ox-DNA was also opened in ChimeraX (PDBID: 1EBM) and superimposed onto the NLRP3 pyrin domain. The hOGG1 structure was hidden, leaving the ox-DNA and the electrostatic potential map.

QUANTIFICATION AND STATISTICAL ANALYSIS

A one-way ANOVA was used to conduct all statistical analyses herein with the exception of the analysis of the 8-oxo-dG ELISA on the cytosol and supernatant DNA from wild-type and NLRP3 knockout iBMDMs, which were analyzed using a two-way ANOVA. All statistical analyses were performed as indicated in the figure legends where N represents the number of replicates. The data all represent mean $\pm$ SEM where p-values <0.05 were considered statistically significant.